DOE/ID/13324--71

Steel Penetration in Sand Molds

Final Technical Report

September, 1994 - September, 1997

Cooperative Agreement
DE-FC07-94ID13324

K.D. Hayes, M. Owens, J. Barlow, D.M. Stefanescu,
A.M. Lane, and T.S. Piwonka

December 1, 1997

The University of Alabama
Tuscaloosa, Alabama

DISCLAIMER

2. Literature Review

While penetration can be divided into different categories depending on the cause of the defect, it should be realized that several factors may have a synergistic effect when combined. The requirements for penetration to occur are described by Equation 2.1.[1,2,3]

$$P_{pen} = \frac{2\sigma\cos\theta}{r_p} \qquad (2.1)$$

Where P_{pen} is the penetration pressure (dynes/cm^2), σ is the surface tension of the liquid metal (dynes/cm), θ is the contact angle between the liquid metal and the substrate material used for the mold (degrees), and r_p is the pore size of the mold material (cm).

Causes of penetration can include too large of GFN, loosely packed sand, or impurities in the metal that lower the contact angle. Penetration can be classified as mechanical or chemical depending on the nature of its cause. Factors such as metallostatic head, particle size, and packing of the sand that affect mechanical penetration are covered thoroughly elsewhere.[4,5,6,7,8]

Chemical penetration results when a chemical reaction produces a change in one of the variables above, ultimately leading to penetration.[9] As an example, penetration can occur if oxygen is present in the mold because FeO, produced in Reaction 2-1, has a lower contact angle (21°) than that of Fe (154.5°) on a silica substrate.[10,11] This change in the value of θ in Equation 1 may cause penetration to occur, depending on the values of the other variables. FeO is able to wet the silica and penetrate, followed by the penetration of iron which wets the iron oxide. In addition, iron oxide may react with sand to form fayalite (Fe_2SiO_4) as shown in Reaction 2-2. The dissolution of silica from the sand grains increases the pore size which also enhances penetration.

Reaction 2-1 $\quad Fe + O_2 \rightarrow 2FeO$

Reaction 2-2 $\quad 2FeO + SiO_2 \rightarrow Fe_2SiO_4$

It has been shown that the purging of molds with oxidizing gases does enhance penetration while purging with neutral and reducing gases inhibits penetration, presumably by enhancing the production of oxides in the former case or decreasing their production in the latter.[12] Rather than purging molds with known gases the composition of the gases produced under foundry conditions may be determined to predict the likelihood of chemical penetration. In previous experiments gases have been collected from the mold-metal interface during casting for later analysis by gas chromatography. The primary gases investigated are CO_2, O_2, CO, CH_4, N_2, and H_2 because these are normally the only gases produced in significant quantities.[13,14,15,16]

Recent experiments with cast iron were performed using a mass spectrometer to determine the gas composition at four second intervals from the initial time of casting

through solidification.[17] These experiments showed that chemical penetration does not occur with cast iron in green sand molds. This is because the high concentration of C in cast iron provides sufficient quantities of the sacrificial element to prevent the oxidation of Fe.[18] Pouring temperatures have also been found to affect the oxidizing abilities of mold gases with some mold materials.[19] This is presumably due to the vaporization of more organic material contained in the mold. This is the same reason that seacoal additions are generally made to green sand molds. The extra carbon contained in the mold reacts with oxidizing gases to produce a more reducing environment. This could also be one of the factors making resin bonded molds effective in preventing penetration. Seacoal also tends to swell when heated, thereby decreasing the pore size of the mold and making it harder for mechanical penetration to occur.[20]

Silica can be dissolved by steam according to Reaction 2-3.[21] This reaction is forced to the right by oxidation reactions that consume O_2 to produce CO, CO_2, FeO and H_2O. Thus, carbon additions may reduce the oxidation of iron only at the cost of increasing the quantity of silica dissolved by steam.

Reaction 2-3 $\quad SiO_2(s) + 4H_2O(g) \rightarrow SiO{\cdot}4H_2O(g) + \frac{1}{2}O_2(g)$

FeO and Fe_2SiO_4 have lower melting points than iron or silica which means that the production of fayalite and penetration may occur even after the casting has solidified.[22] Fayalite is often found on the surface of castings with penetration defects, and its presence is taken as sufficient evidence that the penetration is chemical in nature. In some cases, the fayalite separates easily and actually aids in shakeout while in others it is firmly attached and presents a removal problem.

The penetration produced on steel castings can vary from casting to casting. In some cases the material is extremely difficult to remove and may require expensive grinding operations to make it serviceable. In other castings the formation of fayalite has actually been found to increase the ease of shakeout. This may be due to differences in the composition of the oxidation products. Oxide layers composed of a mixture of FeO, Fe_2O_3, and MnO separate have been found to separate easily from iron because of their different coefficients of expansion while oxides composed purely of FeO adhere more tightly.[23]

Oxides of other metals may also be formed on the casting surface depending on the composition of the metal cast. Alloys of high Mn content pose problems because of the preferential oxidation of Mn leading to a low melting point silicate which produces a casting with strongly adhering sand.[24] These silicates have been identified as $MnSiO_3$ and $MnSiO_4$.[25]

The effect of different elements on such characteristics as contact angle is taken into consideration when formulating mold coating materials. A study of chromite showed that in addition to its ability to swell to seal surfaces and its resistance to attack by iron oxide it is not wetted by steel.[26,27] The characteristics of several mold and core coatings

3. Case Study of Steel Penetration in Sand Molds

3.1. Introduction

As an initial stage to determine the causes of penetration in steel castings, samples of penetration were submitted by the industrial sponsors and penetration samples were taken from castings poured at the University of Alabama. The pouring conditions, compositions, and mold and core characteristics were recorded. Metallographic specimens of the penetration samples were prepared, and both optical and SEM analysis of the samples were performed.

3.2. Materials Studied

Table 3-1 shows the casting description and pouring conditions for the industrial samples of penetration supplied by the sponsors. Table 3-2 lists the chemical compositions of the penetration samples. Samples 4, 6, 7, and 13 are stainless steels, and the remaining samples are low alloy steels. Table 3-3 lists the mold and core conditions for the penetration samples. Table 3-4 lists the molding and pouring conditions of the samples poured at the University of Alabama along with any comments. Table 3-5 lists the compositions (all are plain carbon steels) of the samples poured at the University of Alabama. Samples with an UA in the number designate samples poured at the University of Alabama.

Table 3-1. Casting description and pouring conditions for case study of steel penetration.

No.	Casting description	Casting weight (lb)	Metallostatic head (in.)	Defect frequency (%)	Pouring ladle	Pouring temp. (°F)
1	Rectangular box w/ cores	800	N/A	N/A	3000 lb. Bottom pour, 1.5" nozzle	N/A
2	Ring	2900	N/A	N/A	8000 lb.	N/A
3	Valve wafer body	2270	N/A	N/A	Bottom pour, 2" nozzle	N/A
4	Bonnet	N/A	14 - 36	>50	Bottom pour, 1.5" nozzle	2800-2810
5	N/A	N/A	43	100	Bottom pour, 1.5" nozzle	2840-2880
6	Blade ring	12500	43	100	N/A	2820
7	Ring	N/A	5 - 7	40	1000 lb. teapot	2825
8	N/A	N/A	12	First time	9000 lb. bottom pour with 2" nozzle	2800
9	Carrier	87	5 - 7	<5	600 lb. teapot	2925
10	Pin	193	8 - 10	<50	600 lb. teapot	2825
11	Pin	140	8 - 10	<25	600 lb. teapot	2875
12	Valve	203	8 - 10	<75	600 lb. teapot	2925
13	Ring	N/A	20	2	N/A	2800

Table 3-3. Mold and core characteristics for case study of steel penetration

No.	Mold			Core		
	sand	**coating**	**binder**	**sand**	**coating**	**binder**
1	60 GFN NJ Silica	Sprayed alcohol/zircon	1.5% Pep-Set	60 GFN NJ Silica	Brushed alcohol/zircon	1.5% Pep-Set
2	Silica	N/A	N/A	Silica	N/A	N/A
3	Silica	N/A	N/A	Silica	N/A	N/A
4	60% reclaim/40% new silica or 50% zircon/50% new silica	Sprayed alcohol/zircon	1.5% Pep-Set or 0.9% Pep-Set	60% reclaim/40% new silica or 50% zircon/50% new silica	Brushed alcohol/zircon	1.5% Pep-Set or 0.9% Pep-Set
5	55-58 GFN W&D silica & 3% black Fe oxide (magnetite)	1st coat: brushed alcohol/zircon; 2nd coat: sprayed alcohol/zircon	1.1% Phenolic Urethane No-Bake (60:40) and 3.5% catalyst	N/A	N/A	N/A
6	N/A	N/A	N/A	zircon	none	Baked for 1 hr
7	60 GFN Reclaimed	Sprayed Alcohol mold wash	No Bake	N/A	N/A	N/A
8	60 GFN Silica 60% Reclaim 40% new	Alcohol Zircon (Brushed)	Pep-Set	N/A	N/A	N/A
9	70 GFN Silica, 4% Iron Oxide (2% reg., 2% Sperox), 2.5% Kiln Clay	Vinsel, wax, low hexa	4.5% Resin (Shell)	70 GFN Silica, 4% Iron Oxide, 2.5% Kiln Clay	Sprayed water/zircon	4.5% Resin
10	70 GFN Silica, 4% Iron Oxide (2% reg., 2% Sperox), 2.5% Kiln Clay	Vinsel, wax, low hexa	4.5% Resin (Shell)	No Core		
11	70 GFN Silica, 4% Iron Oxide (2% reg., 2% Sperox), 2.5% Kiln Clay	Vinsel, wax, low hexa	4.5% Resin (Shell)	70 GFN Silica, 4% Iron Oxide, 2.5% Kiln Clay	None	4.5% Resin
12	53 GFN Lake Sand	Brushed water/zircon	1% Furan 941, 25-30% catalyst (binder (Sulfonic Acid))	53 GFN Lake Sand	Brushed water/zircon	1% Furan 941, 25-30% catalyst (binder (Sulfonic Acid))
13	60 GFN: 60% Reclaimed, 40% New Silica	Sprayed Alcohol/Zircon	1.5% Pepset	60 GFN: 60% Reclaimed, 40% New Silica	Brushed Alcohol/Zircon	1.5% Pepset

Table 3-4. Molding and pouring conditions for samples poured at University of Alabama.

No.	Sand	Coating	Binder	Pouring Temp., °F	Penetration	Comments
UA1	Silica; 71 GFN	None	1.5% Pep-Set		No	Cold Metal
UA2	ABC	Brushed Zircon	Sodium Silicate	2842	No	
UA3	Eagle	Brushed Zircon	Furan	2798	No	
UA4	ABC	Brushed Mullite	Sodium Silicate	2857	No	
UA5	ABC	None	Sodium Silicate	2863	Chemical	
UA6	Eagle	Mullite	Furan	2836	No	
UA7	ABC	Brushed Magnesite	Sodium Silicate	2837	Chemical	Slag in Metal
UA8	Eagle	Magnesite	Furan	2870	No	
UA9	Silica; 71 GFN	None	6% Western Bentonite, 4% Water, 4.9% Seacoal	2876	Chemical	
UA10	Silica; 71 GFN	Brushed Magnesite	6% Western Bentonite, 4% Water, 4.9% Seacoal	2776	Chemical	Bad Coating
UA11	Eagle	None	Furan	2785	Chemical	
UA12	Silica; 71 GFN	Brushed Zircon	6% Western Bentonite, 4% Water, 4.9% Seacoal	2896	No	
UA13	Silica; 71 GFN	Brushed Mullite	6% Western Bentonite, 4% Water, 4.9% Seacoal	2846	No	
UA14	Silica; 71 GFN	None	6% Western Bentonite, 4% Water, 4.9% Seacoal		Chemical	
UA15	Silica; 71 GFN	None	5% Sodium Silicate	2930	Chemical	
UA16	Silica; 71 GFN	None	1.5% Pep-Set	2942	No	
UA17	Silica; 71 GFN	None	6% Western Bentonite, 4% Water	2961	Chemical	
UA18	Silica; 71 GFN	None	6% Western Bentonite, 4% Water, 4.9% Seacoal	2933	Chemical	
UA19	Silica; 71 GFN	None	5% Sodium Silicate	2903	Chemical	
UA20	Silica; 71 GFN	None	5% Sodium Silicate	3083	Chemical	

Table 3-7. Compositions obtained for penetration samples by using WDS.

Sample #	Region	Composition wt%					Composition at%				
		Fe	Mn	Si	Cr	O	Fe	Mn	Si	Cr	O
5	1	98.37	0.63	0.56	0.15	0.29	97.11	0.64	1.10	0.16	0.99
5	2	0.61	0.02	44.25	0.04	55.08	0.22	0.01	31.32	0.01	68.44
5	3	45.24	4.98	16.81	0.06	32.91	22.77	2.55	16.83	0.03	57.82
5	3	51.30	2.91	13.55	1.18	31.05	26.88	1.55	14.12	0.67	56.79
5	4	23.54	2.17	32.34	0.09	41.86	9.96	0.94	27.22	0.04	61.84
5	5	74.11	0.22	0.16	0.06	25.44	45.32	0.14	0.20	0.04	54.30
7	1	98.16	0.40	0.88	0.02	0.54	96.03	0.39	1.71	0.02	1.85
7	5	71.23	0.39	0.00	0.04	28.34	41.75	0.24	0.00	0.02	57.99
7	5	73.12	0.20	0.03	0.00	26.66	43.93	0.12	0.03	0.00	55.92
7	5	69.03	1.61	1.75	0.01	27.61	40.49	0.96	2.04	0.01	56.51
7	6	23.69	11.13	25.39	0.22	39.56	10.58	5.06	22.56	0.11	61.69
9	1	98.48	0.70	0.55	0.01	0.27	97.28	0.70	1.08	0.01	0.93
9	5	74.63	0.77	0.00	0.00	24.59	46.28	0.49	0.00	0.00	53.23
9	6	44.92	2.91	15.87	0.04	36.26	21.81	1.44	15.32	0.02	61.42
9	9	72.74	0.98	1.25	0.33	24.70	44.68	0.61	1.53	0.22	52.96
10	1	98.50	0.61	0.57	0.06	0.26	97.31	0.62	1.12	0.06	0.90
10	3	52.48	0.80	14.65	0.00	32.07	27.00	0.42	14.99	0.00	57.60
10	5	76.37	0.33	0.03	0.03	23.25	48.36	0.21	0.03	0.02	51.38
10	5	73.43	0.29	0.17	0.13	25.98	44.54	0.18	0.21	0.08	55.00
11	1	97.96	0.90	0.75	0.09	0.31	96.48	0.90	1.47	0.10	1.06
11	2	2.52	0.14	46.33	0.00	51.00	0.92	0.05	33.77	0.00	65.26
11	2	1.55	1.61	41.45	0.00	55.39	0.56	0.58	29.55	0.00	69.31
11	5	69.22	3.68	1.14	0.22	25.73	41.88	2.27	1.38	0.14	54.34
14	1	98.27	0.67	0.73	0.12	0.22	97.04	0.66	1.43	0.13	0.74
14	3	51.56	0.85	14.79	0.00	32.80	26.27	0.44	14.98	0.00	58.32
14	4	20.38	0.71	29.49	0.05	49.39	8.08	0.28	23.26	0.02	68.36
14	5	75.58	0.22	0.09	0.07	24.04	47.24	0.14	0.12	0.05	52.45

3.3.1. Low alloy steels

The low alloy samples 1, 2 and 3 displayed an oxidized region (region 2) where the compositions did not vary significantly from the unoxidized matrix (region 1) as shown in Table 3-6, Fig. 3-1, and Fig. 3- 2(a) (Energy-dispersive x-ray spectrometry (EDS) on this SEM cannot detect the presence of oxygen.). Samples 1, 2, and 3 also displayed a region at the interface

a) 25X

Fig. 3-1. Optical microstructures of chemical penetration region, sample 2, low alloy steel.

(region 3) which is rich in silica (Table 3-6 and Fig. 3-1 and Fig. 3-2(a)). This layer is most probably fayalite. This indicates chemical penetration in the samples.

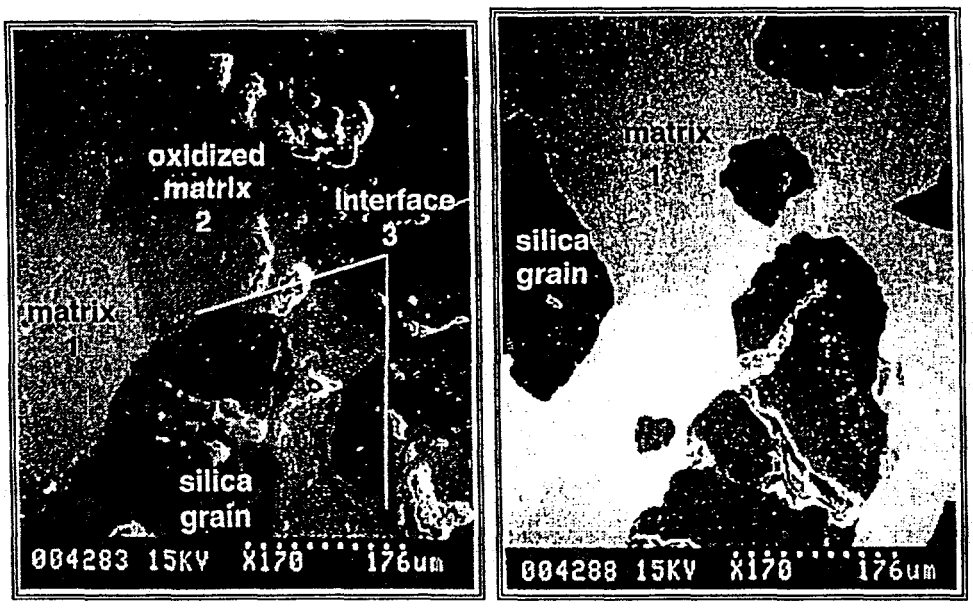

(a)sample 2, low alloy steel **b) sample 4, stainless steel**

Fig. 3-2. SEM picture of penetration regions.

When combined with the WDS data from the UA samples, the assumptions of the exisistence of an oxidized layer and a fayalite region are confirmed. All compositions for the following

regions are shown in Table 3-7. As shown in Fig. 3-3, Region 1 is the base metal composition for the castings. Region 2 is the sand grain which is obviously silica. Region 3 for the light phase of the eutectic region also is fayalite. Region 4 is the dark eutectic region. This is a silica rich region of the eutectic. Region 5 is the oxidized region (FeO) as in castings 9 and 10.

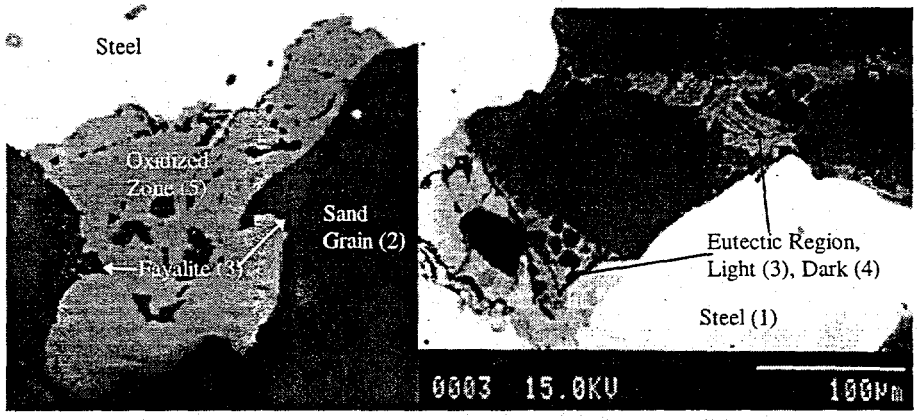

(a) (b)

Figure 3-3. Photomicrograph (a) and back-scattered electron micrograph of casting #UA5 showing chemical penetration zone and interfacial region.

Chemical penetration also occurred in the uncoated green sand samples. The three castings in green sand (Castings #UA9, #UA10, and #UA14) that exhibited penetration had nearly identical surface defects, as shown in Figure 3-4. There is a reaction zone at the surface of the casting and around the pores at the interface. As can be seen in Figure 3-4(b), there are actually three parts to the reaction zone. Some of the pores contained a small amount of sand. The casting that had a magnesite coating was not applied properly and was too thin. This led to mold erosion where sand grains became entrapped in the molten metal, instead of the metal penetrating in between the sand grains.

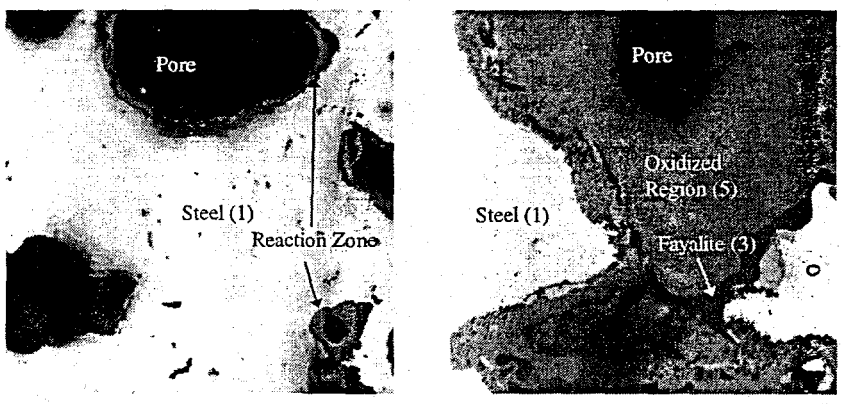

(a) 50 (b) 400x

Figure 3-4. Photomicrographs of casting #UA10, showing the typical microstructure of the green sand castings that exhibited penetration.

The iron oxide-silica phase diagram is shown in Fig. 3-5. This shows the existence of two eutectics which is what is observed in the penetration samples. These are eutectics between iron

oxide and fayalite and fayalite and silica. These regions are sometimes difficult to see under a light microscope, so the sample must be studied carefully to observe the regions in some cases.

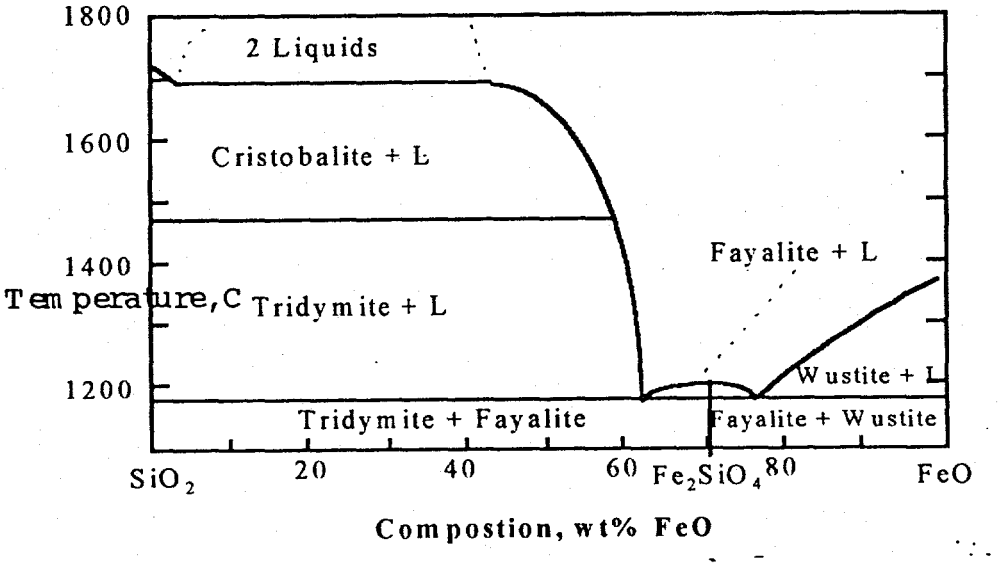

Figure 3-5. Iron Oxide-silica phase diagram [35]

The other low alloy steels displayed no oxidized region. This would indicate that some type of mechanical penetration occurred. Fig. 3-6 shows a typical region of mechanical penetration. For sample 10 this can be attributed to a coating failure (Figure 3-7). The metal outside of the coating appears the same as that on the interior of the casting as shown in Figure 3-7. This indicates that the metal penetrates the coating but not the mold.

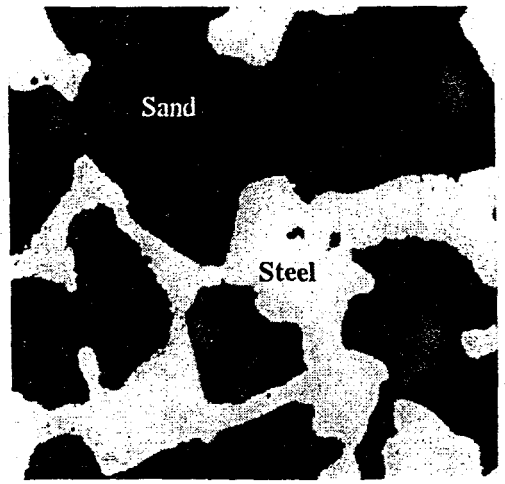

Figure 3-6. Optical microstructure of low alloy steel where no chemical penetration is present (Sample 8, 100x).

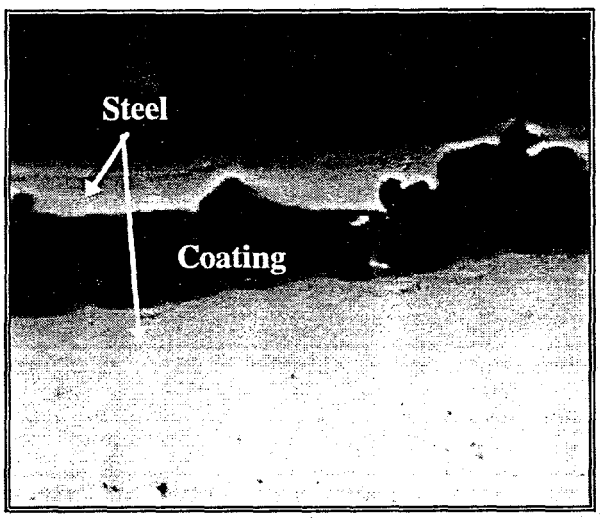

Figure 3-7. Optical microstructure showing a coating failure (Sample 10, 25x).

The composition of sample 10 was checked on the microprobe using wavelength dispersive spectrometry (WDS). This is the sample where a coating failure was observed. The results are given in Table 3-8. Carbon can be detected by WDS, but the results are not reliable because it is close to the detection limit. The Mn content in the layer (region 2) is somewhat less than the bulk composition (region 1), while the Si content exhibits the opposite trend. The Cr, Ni, and Mo contents do not vary significantly with position.

Table 3-8. Composition of sample 10 using both spectral analysis and WDS.

Type of Analysis	Measurement Position		Composition wt%					
	No.	Description	C	Mn	Si	Cr	Ni	Mo
Spectral	1	Bulk	0.25	0.80	0.50	0.60	0.65	0.20
WDS	1	Bulk	-	0.77-0.82	0.55-0.56	0.64-0.76	0.59-0.65	0.0-0.29
WDS	2	Layer	-	0.55-0.61	0.85-0.90	0.67-0.72	0.58-0.71	0.13-0.38

The penetration sample for casting #15 was examined using an SEM where detection of the oxygen content was possible. As shown in Figure 3-8a, casting #15 had a penetrated region next to the base metal as well as an attached layer which could be removed using considerable force. The regions on the sample were studied using EDS. The results are shown in Table 3-9. Next to the steel there are regions which contain the base metal (steel), iron oxide, fayalite, and silica. The compositions of each of these are shown in Table 3-9 (The oxygen content registered consistently high for all substances which contained it, *i.e.* silica should have been 66.7 at% O and 33.3 at% Si.). These are much like values previously obtained in this work. However, in the outside penetrated region there is a difference from previous samples. Shown in Figure 3-8c is the silica and fayalite phases previously observed on the samples. However, the silica (dark regions) are actually two phases. The lighter phase contains more sodium, iron, and aluminum than the darker phase. The darker phase could be nearly pure silica where the interaction volume of the beam also strikes the lighter silica phase when examined. The importance of this is that sodium from the sodium silicate binder affected the composition of the penetrated region. This could also aid in the penetration mechanism.

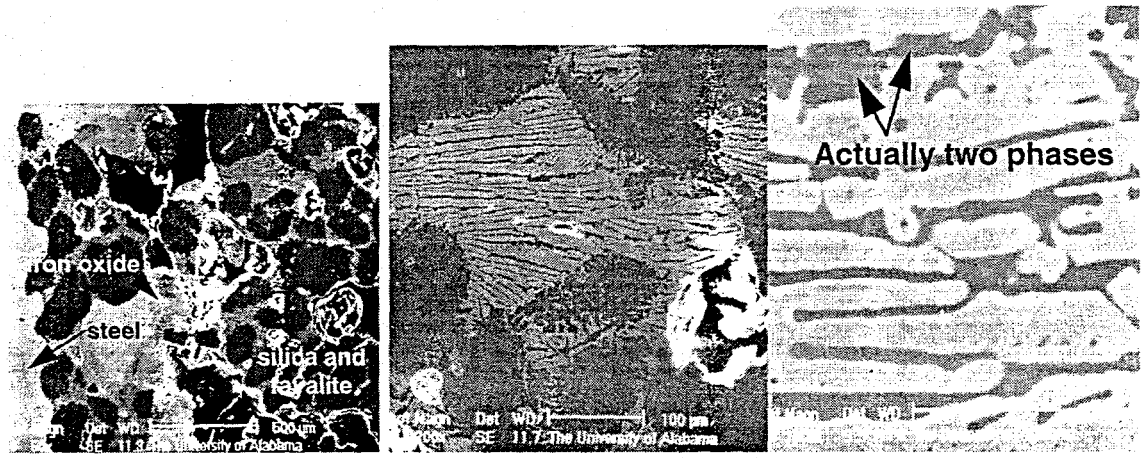

(a) 50x (b) 200x (c) 1600x

Figure 3-8. Electron micrographs of casting #15 showing (a) the entire penetrated region, (b) a higher magnification of the attached layer of fayalite and silica, and (c) an even higher magnification showing the sodium containing phases and fayalite (the lightest phase).

Table 3-9. EDS results from examination penetrated region of casting #15.

	Composition, at%						Composition, wt%					
Area	O	Si	Fe	Mn	Al	Na	O	Si	Fe	Mn	Al	Na
Steel	ND	0.8	99.2	ND	ND	ND	ND	0.4	99.6	ND	ND	ND
Iron Oxide	65.8	0.7	33.5	ND	ND	ND	36.8	0.7	63.5	ND	ND	ND
Fayalite	70.5	10.6	17.7	0.7	0.5	ND	45.8	12.1	40.0	1.5	0.6	ND
Sand	75.4	24.6	ND	ND	ND	ND	63.6	36.4	ND	ND	ND	ND
Silica Dark	74.5	22.8	0.8	ND	0.7	1.2	62.0	33.2	2.3	ND	1.0	1.5
Silica Light	72.1	17.9	4.1	ND	1.7	4.2	56.9	24.9	11.2	ND	2.3	4.8

ND=Not detected.

3.3.2. Stainless steels

The stainless steel samples did not display the oxidized region or the layer at the interface, as shown in Table 3-6 and Figure 3-2b. This indicates mechanical penetration in the stainless steel samples. The reason for this is that the chromium present in the stainless steels protects the iron from oxidation. Sample 7 also penetrated due to a coating failure as in sample 10 (Figure 3-7).

4. Sessile Drop Experiments

4.1. Experimental Method

The experimental method used is similar to that used by Stefanescu et al[36,37] for determining the contact angles for cast iron on various molding substrates.

4.1.1. Equipment

The experimental apparatus used for the sessile drop experiments is a Centorr Model 15 vacuum furnace that is capable of obtaining a vacuum of 10^{-5} to 10^{-6} Torr. The atmosphere can be either vacuum or an inert gas, and the maximum operating temperature is approximately 2500 °C.

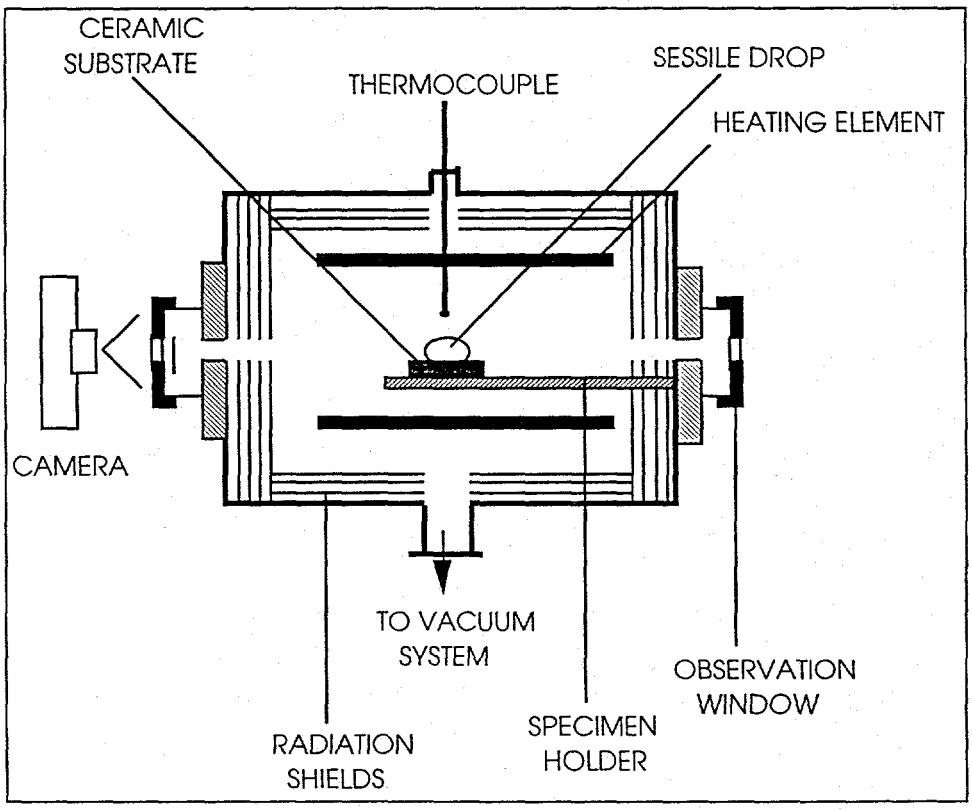

Figure 4-1 Centorr model 15 vacuum furnace used for sessile drop experiments.

4.1.2. Procedure

Samples of steel were obtained from the industrial sponsors. These samples were then turned on a lathe to obtain 5 mm diameter rods. These rods were sectioned into 5 mm long cylinders on a low-speed diamond saw.

The substrate were then prepared for the experiment. If a particulate substrate was used, the substrate was compacted into a circular alumina dish (30 mm dia. x 6 mm in height) and struck flat by a razor blade. Some of the particulate substrates also required a sintering and grinding

operation due to deformation of the substrate upon heating, which prevented an accurate measurement of the contact angle. The substrates were heated in a tube furnace to a temperature of approximately 1525 °C at a rate of 200 °C/hr, held for 45 min., and cooled to room temperature at a rate of 100 °C/hr. The sintered disc was then removed from the alumina dish and ground in successive steps from 120 grit to 600 grit using silicon carbide grinding paper. The ground discs were then cleaned using compressed air. For monolithic substrates, a quarter of a 40 mm dia. disc or a whole 20 mm dia. disc of the substrate was used, depending upon availability. The specimen was placed onto the specimen stage and leveled by placing a bull's-eye level on the substrate surface.

The sample was then hand ground on 240 grit silicon carbide (SiC) paper to remove any machine marks. Any oxidation is removed by hand polishing on 600 grit SiC paper followed by 4/0 emery paper both under 97% isopropyl alcohol. The sample was then immediately placed on the substrate and sealed in the furnace. The furnace chamber was then pumped down to less than $2x10^{-4}$ Torr, and then filled with 4.8 grade argon. The argon was allowed to flow for 5 min. This process was repeated twice to ensure that most of the air was removed from the chamber.

The furnace temperature was then increased to the melting point (with the argon flowing), and this temperature was recorded. The temperature was raised to the prescribed superheat (based on the melting point obtained for the experiment) in approximately 5-7 min

Pictures were taken every 3 min. for 33 min. using a 20X lens on a 35 mm camera that was leveled using the bull's-eye level on the tripod. The temperature was recorded at each photograph. The normal variation in temperature was approximately ±1 °C.

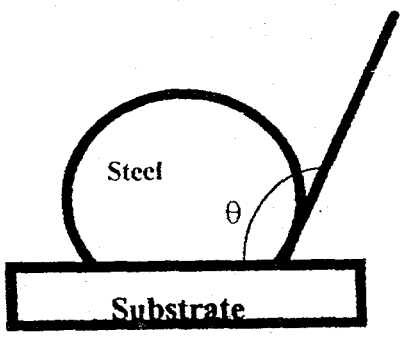

Figure 4-2. Measurement of a contact angle from a sessile drop experiment.

The photographs were scanned into a computer and magnified approximately 6X. The contact angles of both the left and the right sides of the drop were measured using ClarisDraw© software. This was done by drawing a reference line at the bottom of the drop and then a tangent line from the apex of the angle and obtaining the angle of the line, as shown in Figure 4-2. The computer software displays the angle of the line.

4.2. Materials Tested

A number of sessile drop experiments involving steel of various composition and different refractory substrates were performed. The steel samples included carbon steel, high manganese steel, and stainless steel. These compositions are shown in Table 4-1

Table 4-1. Compositions steel of samples used for sessile drop experiments.

Sample	Source	Composition													
		C	Si	Mn	P	S	Cr	Al	V	Ni	Sn	Mo	Cu	Ti	Other
76 Plain C-2	ABC	0.76	0.57	0.72	0.023	0.017	0.08	0.04	0.003	0.03	0.003	0.006	0.050	0.002	
76 Plain C-4	ABC	0.76	0.63	0.73	0.023	0.016	0.08	0.05	0.003	0.03	0.002	0.005	0.050	0.002	0.001 B
High Mn	ABC	1.08	0.78	13.23	0.340		0.31	0.26							
Stainless Steel	PA	0.08 max	2.0 max	1.5 max	0.04 max	0.04 max	18 - 21			9 - 12		2 - 3			
0.1 Plain C	Eagle Alloys	0.10	0.40	0.46	0.018	0.011	0.06	0.04	0.003	0.03		0.004	0.029	0.004	0.001 Zr
0.27 Plain C-2	ASF	0.27	0.38	0.77	0.015	0.021	0.14	0.07	0.001	0.06	0.006	0.030	0.080	0.004	

* Balance Fe

The substrates and the average particle diameters (determined by wet laser particle size characterization) and applicable grain fineness numbers (GFN's) are given in Table 4-2, and Table 4-3 gives the compositions of the substrates. The substrates include: silica (SiO_2), zircon ($ZrSiO_4$), olivine, three alumina level mullites (Al_2SiO_5), calcined bauxite ($\approx 90\% Al_2O_3$-SiO_2), alumina (Al_2O_3), chromite (Mg_2SiO_4-Fe_2SiO_4), and magnesite. All of the sessile drop experiments were performed with either a superheat of 150 °C or 50 °C and in an 4.8 grade argon atmosphere.

Table 4-2. Substrates used in sessile drop experiments.

Substrate	Average Particle Diameter (μm)	GFN
Monolithic Quartz	-	-
Zircon Flour	18.9	-
Zircon Sand	152	115
Magnesite Flour	14.6	-
Coarse Magnesite	25.3	-
Olivine Sand	115.6	-
Olivine Flour	59.9	-
Chromite Sand	316	56
Chromite Flour	27.7	-
Mulcoa 60-20 (Mullite Sand)	316	61
Mulcoa 60-325 (Mullite Flour)	28.5	-
Mulcoa 70-325 (Mullite Flour)	29.8	-
Mulcoa 70-20 (Mullite Sand)	340	58
Calcined Bauxite Flour (325 mesh)	15.0	-
Calcined Bauxite Sand (20 mesh)	324	54
High Density Alumina	-	-

Table 4-3. Compositions of selected substrates tested.

Substrate	Composition wt%							
	Al_2O_3	SiO_2	TiO_2	Fe_2O_3	CaO	MgO	Na_2O	K_2O
Mulcoa 60	59.2	37.3	2.11	1.13	0.06	0.07	0.07	0.04
Mulcoa 70	69.2	26.6	2.77	1.22	0.06	0.08	0.07	0.05
Calcined Bauxite	88.5	6.2	3.5	1.3				
High Density Alumina	99.5							

4.3. Results

4.3.1. Sand Aggregates

Results of the sessile drop experiments were fit to a second order polynomial of the form:

$$\theta = A + Bt + Ct^2 \tag{3.1}$$

where A,B, and C are constants and t is time. This data is needed so the contact angle can be calculated for a given solidification time of the casting. Another way of specifying the contact angles can be as either the maximum contact angle or the steady state contact angle. Since large castings take longer to solidify, the steady state value should be used for them and the maximum angle should be used and for small castings.

The contact angles for monolithic substrates were merasured for several substrates. Fine and coarse substrates are needed to determine the contact angle for a particulate substrate.[37] The contact angles for particulate substrates were determined using the average particle diameters for the coarse and fine grained substrates and extrapolating to a particle diameter of zero. This particle diameter of zero corresponds to a zero fraction of voids

4.4. Discussion

4.4.1. Influence of type of steel and substrate

The contact angles for each alloy varied depending on the substrate it was tested on. Most carbon steel experiments result in a non-wetting contact angle. However, the stainless steel and the high manganese steel display a wetting behavior on a number of substrates. The varied contact angles on the quartz substrate can be used as an example. One carbon steel sample exhibited an average contact angle of approximately 100°. This angle is slightly non-wetting, which implies that this alloy may be susceptible to mechanical penetration in silica molds. The stainless steel sample had an average contact angle of 83°. This is slightly wetting which implies that this alloy would be susceptible to mechanical penetration in a silica sand. The high manganese steel had an very wetting contact angle of less than 20°. The angle became wetting

immediately after melting (at approximately 1 minute after melting the contact angle was 51°). Penetration will certainly occur when pouring this alloy into silica molds with no coating.

The substrate for the high Mn steel on quartz sessile drop experiment was also studied on the SEM. Figure 4-3 shows the micrographs. On the micrographs are the quartz substrate, a porous region of silica, silica dendrites, and $MnSiO_3$. The results of the EDS work are shown in Table 4-4. Results of EDS examination of phases found on the quartz substrate after running a high Mn steel sessile drop experiment.. The quartz substrate had the composition of pure silica as expected (note that the oxygen level is high). The region of porous silica also contains some aluminum. The silica dendrites were nearly pure silica. However, the interdendritc region had significant amounts of Mn (nearly equal amounts as Si, atomically), leading to the conclusion that the region is the low melting point phase $MnSiO_3$ which is much like fayalite. The only source of oxygen in the sessile drop furnace is the silica in the substrate, therefore the Mn reduced the silica to obtain the oxygen. This shows why high Mn steel cannot be poured in silica molds. Also note that no iron was found in the substrate, demonstrating Mn's higher affinity for oxygen.

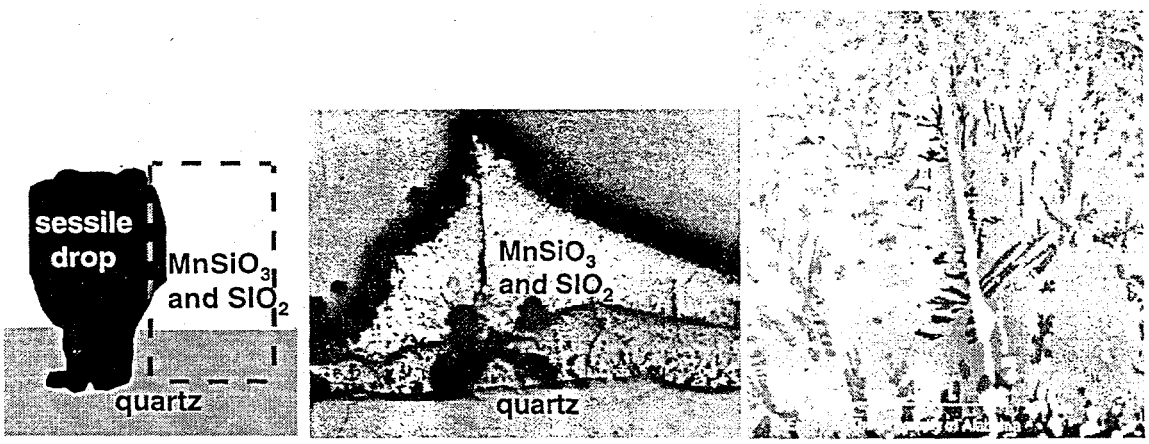

(a) (b) 25x (c) 160x

Figure 4-3. (a) Schematic of the area where the micrographs were taken and micrographs at 25x (b) and 160x (c) showing the substrate.

Table 4-4. Results of EDS examination of phases found on the quartz substrate after running a high Mn steel sessile drop experiment.

	Composition, at%				Composition, wt%			
Area	O	Si	Mn	Al	O	Si	Mn	Al
Quartz Substrate	76.3	23.7	ND	ND	64.7	35.3	ND	ND
Porous Silica	75.1	23.3	ND	1.6	63.3	34.4	ND	2.3
Interdendritic Area	73.8	13.0	12.8	0.4	52.3	16.2	31.0	1.0
Dendrites	76.0	23.6	0.3	0.1	64.0	34.8	1.0	0.2

ND=Not detected

All contact angles decreased with time for all steels on all substrates at 150 °C superheat. This indicates that the alloys are not immediately at equilibrium with the substrate. This trend is

reflected for the all substrates tested. The decrease in contact angle suggests that the alloys are more susceptible to penetration in castings which have a long time before a solid skin forms on the surface.

From all the substrates tested it is apparent that the highest contact angle is given by magnesite or calcined bauxite flour, followed by zircon then the mullites. This makes magnesite and bauxite flour the most effective substrates for the prevention of penetration of any substrate tested. The higher contact angle of zircon as compared to silica demonstrates that it may be advantageous to use zircon sand in areas where penetration is a concern. The olivine sand has a much larger contact angle in contact with high Mn steel than silica does. The olivine sand and flour melted when experiments were performed with stainless steel and carbon steel. Therefore, olivine should only be used with high manganese steels.

The chromite sand tested in this research did not exhibit good wetting characteristics. For all three types of steel the contact angle was smaller than 90°. As shown in Figure 4-4, in-situ penetration occurs in the sand aggregate under the sessile drop. It should also be noted that a reaction occured during the CF8M stainless steel on the chromite flour substrate experiment. This reaction prevented measurement of the contact angle because no drop could be formed. Therefore, it was concluded that chromite should not be used for stainless steels.

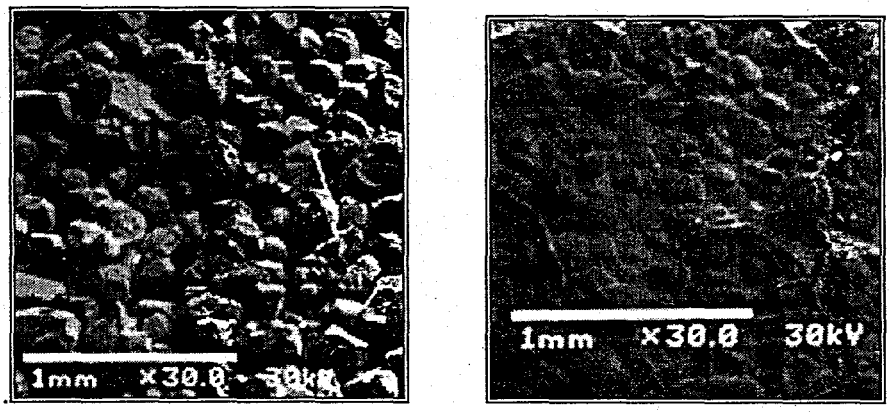

a) next to the sessile drop b) under the sessile drop

Figure 4-4. SEM micrograph of chromite sand grains for 0.76 %C sample.

The effect of superheating temperature varies for different alloys. The effect of the superheat temperature was not significant for the carbon steels when the superheat was decreased to 50 °C. Although there is a slight decrease in contact angle with increasing superheat, this is within the experimental error and cannot be considered significant. However, for the CF8M steel the change was significant. This can be attributed to the borderline wetting-nonwetting behavior of the CF8M steel on the silica substrate. Typically when a sample goes from nonwetting to wetting behavior the contact angle drops significantly (5-10°). As a result of this behavior, lower pouring temperatures would be beneficial for pouring CF8M in silica molds. However, these contact angles are still very low and penetration could easily be seen.

5. Interfacial Gas Compositions of Steel Castings

Experiments were performed to determine if and under what circumstances chemical penetration occurs with steel castings. Castings were poured into molds of different compositions with and without the use of mold and core coatings. Measurements were made of the gas composition at the mold/metal interface. Photomicrographs of casting sections show that unless mold coatings are used chemical penetration will occur with all mold materials tested other than resin bonded molds. The extent of penetration was found to be dependent on the oxidizing ability of the gases produced.

5.1. Experimental Procedure

The experimental set-up is modified from earlier work performed with cast iron.[38] Steel castings were poured in different types of molds: green sand, green sand with no sea coal additions, sodium silicate, Pepset™ and furan. Figure 5-1 shows the placement of probes for the sampling of gases for molds with and without cores. The casting was a cylinder 12" tall with a diameter of 6" which was molded into the cope. A 2" diameter cylindrical core was placed along the vertical axis of the casting. Two 1/16" I.D. stainless steel tubes were placed in the cores of the sodium silicate, Pepset™, and furan molds, at a distance of 1/4" from the casting surface to sample the gases produced. No green sand cores were used in the green sand molds as green sand lacks sufficient strength to be used for cores without added binders. Therefore, the sampling tubes were placed in the drag of the green sand molds at a distance of 1/4" from the bottom of the casting.

The gases produced at the interface were drawn for analysis by gas chromatography (GC) and mass spectrometry (MS) using vacuum. The GC and MS were calibrated with mixtures of the six gases of interest provided to the sample tube inlet prior to their insertion in the mold.

Gases were drawn from a sampling tube through a drying tube packed with calcium carbonate to reduce moisture that might condense and clog the sampling line or increase the background signal of the MS. They were then passed through ~ 6 feet of capillary tubing to reduce the gas flow to ~ 8ml/min. A Leybold Inficon Transpector mass spectrometer was used for analysis. This is a quadrupole instrument using an electron multiplier with a Faraday cup detection system that is capable of measuring mass to charge ratios up to 100.

Gas concentrations were determined for 18 minutes after the introduction of the molten metal to the mold at intervals of four seconds by monitoring 6 different mass/charge ratios. Since the primary gases evolved during casting are CO_2, O_2, CO, CH_4, N_2, and H_2 these were the only gases determined. Water is also present in the mold in high concentrations but presents many problems for analysis. If moisture is allowed to enter the mass spectrometer it tends to stick to the walls of the instrument. The water can then vaporize at a later time increasing the background signal. Water could be detected with the gas chromatograph but often condensed in the sample tube before exiting the mold. For these reasons the gases were determined on a dry basis.

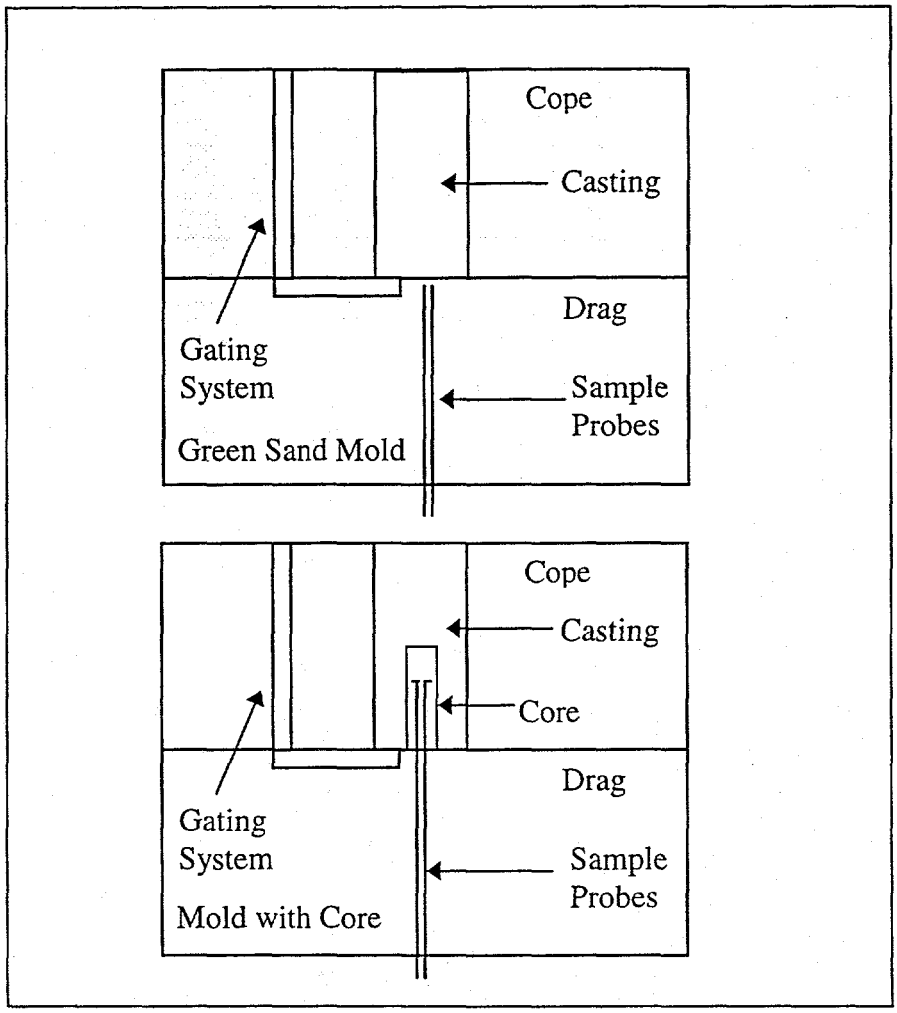

Figure 5-1. Placement of probes for gas sampling in molds and cores.

The mass-to-charge ratios monitored were 44 (carbon dioxide), 32 (oxygen), 28 (carbon monoxide), 15 (methane), 14 (nitrogen), and 2 (hydrogen). The methane concentration was determined by monitoring the signal of CH_3^+ rather than CH_4^+ to eliminate any interference from O^+ or O_2^{++} which was significant because of the water in the system. Nitrogen was determined by monitoring the signal from N^+ rather than N_2^+ to reduce the contribution to the signal from CO^+. The signal for carbon monoxide at 28 was then corrected for the contribution from nitrogen.

The instrument had to be placed a significant distance from the casting which raised two concerns; the mixing of gases and the lag time in detection. Step changes were made in gas concentration at the probe inlet to determine the time constant (τ) of the system. The system was found to have very nearly ideal plug flow with a τ of 45 seconds. The figures showing the gas compositions show the time as detected by the MS.

Gas from the second sampling tube was analyzed with a Hewlett Packard 5890 GC equipped with a thermal conductivity detector. Separation was achieved isothermally at 50 °C with a Haysep D column. A sample collected at approximately 3 minutes after the casting was poured was analyzed for the gases listed above. This required two chromatograms to be run. Analysis of CO_2, O_2, CO, CH_4 and N_2 was performed with a helium carrier while an argon carrier was used for H_2 detection. The GC data was used primarily to verify the MS data.

Cross sections of the castings were viewed optically as well as with a scanning electron microscope to determine the extent and type of penetration present. The photomicrographs of these samples show the presence of iron oxide and fayalite as well as the original steel and sand grains. The areas lightest in color are the original steel sample with iron oxide appearing slightly darker. Fayalite is the next darkest and sand appears almost black. Pores and crevices also appear black and very small bright white spots are thought to be due to foreign material, although they are generally too small to determine with any degree of certainty. The identity of these different shaded areas was determined using Energy Dispersion Spectrometry (EDS).

5.2. Results and Discussion

Our goal was to determine how different mold properties affect the gases produced at the interface and the finish of the casting surface. To best describe the effects of the mold characteristics we first discuss the results obtained from an uncoated green sand mold with seacoal additions. Following this we describe the results obtained when seacoal is omitted from the mold and point out the differences. We continue this process for sodium silicate and resin bonded cores. Finally we discuss the results obtained when these same molds are properly coated with different materials. Properties of the mold for each experiment are listed in Table 2.4. All castings poured at The University of Alabama used molds prepared with silica sand of 71 GFN. This sand was chosen to eliminate mechanical penetration that might occur with a larger grain size. Compositions of the steel for each experiment are listed in Table 3-5. Experiments 1 and 14-18 were performed at The University of Alabama where carbon concentrations were held as closely to 0.28 percent as possible. This low carbon concentration was chosen to increase the probability of producing chemical penetration. Experiments 2-13 were performed at a sponsor's foundry using their normal steel composition with a carbon concentration of approximately 0.7 percent.

Pouring temperatures were held approximately constant to avoid changes in gas composition caused by the vaporization of more organic material with higher temperatures. In experiments 2-13 problems occurred in the collection of gas composition data. The exact cause of the problem was never identified. However, these experiments were performed at a sponsor's foundry where complications included the intermittent loss of electrical power. It is possible that sufficient evacuation of the instrument was never achieved, leading to high background levels of nitrogen, oxygen, and water. Only the casting surfaces are discussed for these experiments.

Two castings were poured in green sand molds that contained seacoal additions (Experiments 14 and 18). In the first of these experiments the overall signal intensities were at background levels for the first minute. Therefore this portion of the data is meaningless and not shown in Figure 5-2. In the second (Experiment 18) the nitrogen and oxygen concentrations drop to

negligible values within less than one minute as seen in Figure 5-3. These gases are flushed from the mold as liquid water is rapidly vaporized to steam. From 1.5 minutes onward the data from both runs look similar. After this time the atmosphere is composed primarily of H_2 and CO which are produced from the reaction between steam and carbon from the mold and from the steel. The oxidizing ability of the atmospheres can be more easily assessed by looking at the CO_2/CO ratios as shown in Figure 5-4 and Figure 5-5. These graphs also have similar appearances for the two runs.

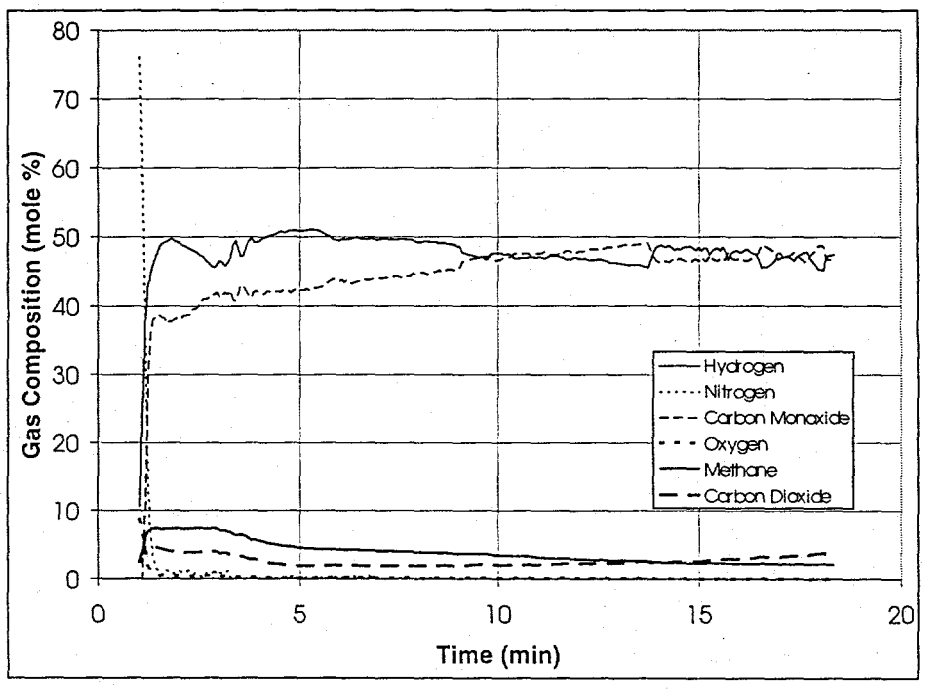

Figure 5-2. Gas composition in a green sand mold, Experiment #14.

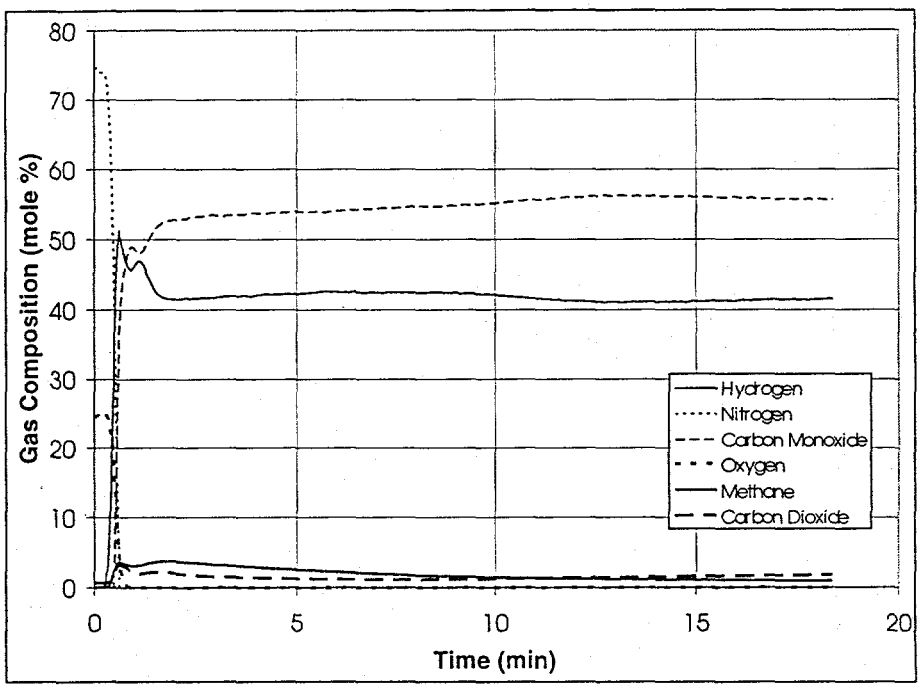

Figure 5-3. Gas compositions in a green sand mold, Experiment #18

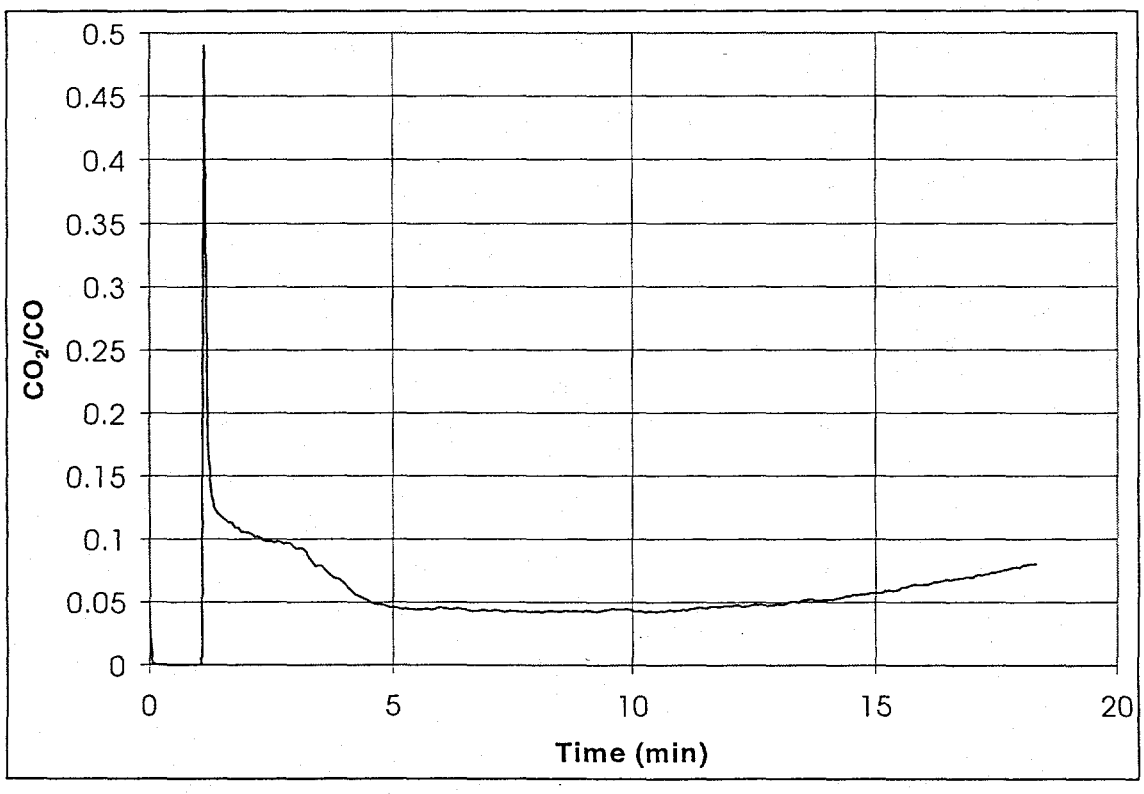

Figure 5-4. CO_2/CO for a green sand mold, Experiment #14.

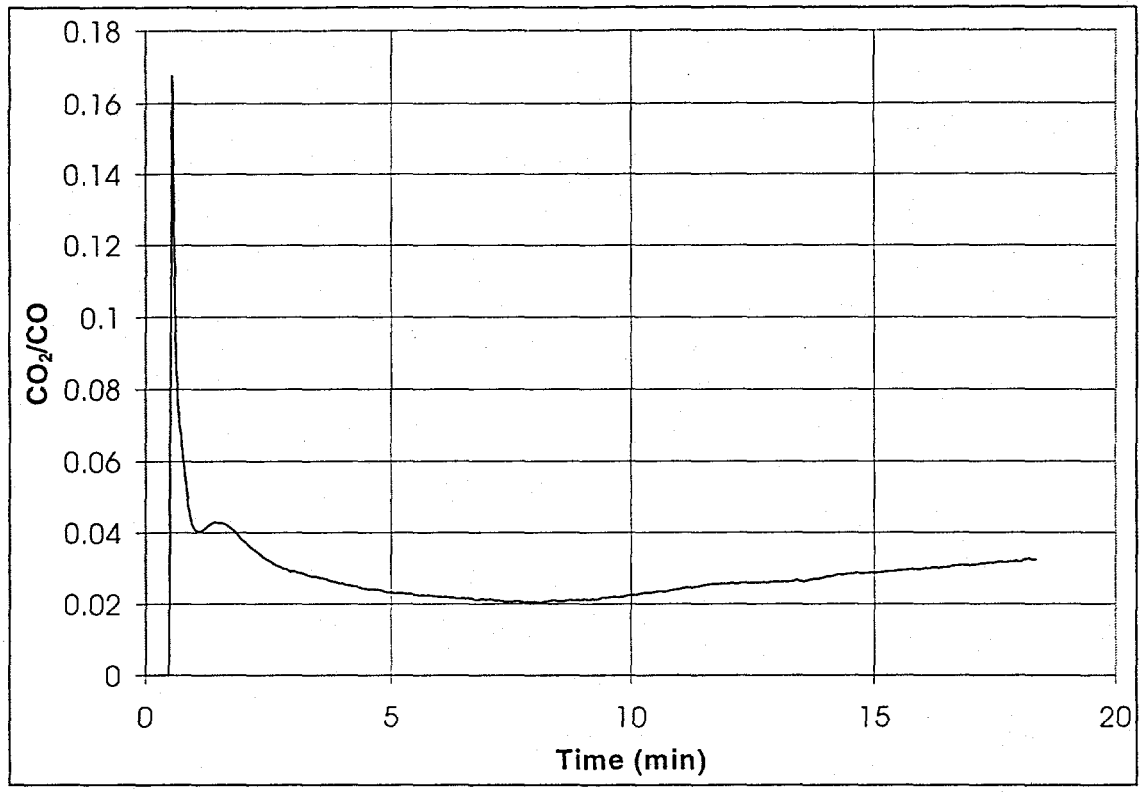

Figure 5-5. CO_2/CO for a green sand mold, Experiment #18.

The CO_2/CO ratio has a low value or is undefined at the beginning of the run, quickly peaks, begins dropping until approximately eight minutes into the run whereupon it again increases gradually through the end of the run. This is what might be expected. Before the casting is poured the concentration of oxygen at the interior surface of the mold is quite high, both in the form of molecular oxygen from air and the oxygen contained in water. When the molten metal first contacts this surface the high temperature causes the rapid vaporization of H_2O which reacts with C to produce CO and, because of the large quantities of oxygen available from the steam, CO_2. It is at this time that CO_2 is produced in the highest concentration. The surface of the casting is quickly blanketed with a layer of H_2 and CO. Now the only source of oxygen is from H_2O which must diffuse inward to the interface. This process is inhibited because of the expansion of gases from the interface fueled by a temperature increase as well as Reaction 5-1 and Reaction 4-2.

Reaction 5-1	$H_2O(g) + C(s) \rightarrow H_2(g) + CO(g)$
Reaction 5-2	$CO_2(g) + C(s) \rightarrow 2CO(g)$

Carbon, in solution, continues to diffuse through the steel uninhibited; therefore, the ratio of CO_2/CO begins to decrease.

It was determined using a solidification model that a solid steel skin begins to form on the surface of the casting after eight minutes into the experiment. This lowers the rate at which

carbon can diffuse to the surface. The temperature of the mold is no longer increasing and Reaction 5-1 and Reaction 45-2 have depleted the available reactants. Because the gases are no longer expanding as rapidly the bulk flux away from the interface begins to decrease. This allows steam to diffuse back to the interface more easily and faster than carbon can diffuse through the solid steel skin to the interface. These two factors cause the CO_2/CO ratio to begin to increase slightly.

Penetration was visible on the surface of both of these green sand castings. The photomicrographs (Figure 5-6, Figure 5-7 and Figure 5-8) show the presence of fayalite which changes the contact angle of steel. Therefore, the penetration is chemical in nature. Apparently, the casting surface only needs to be exposed to an oxidizing atmosphere for a short period of time for penetration to be induced.

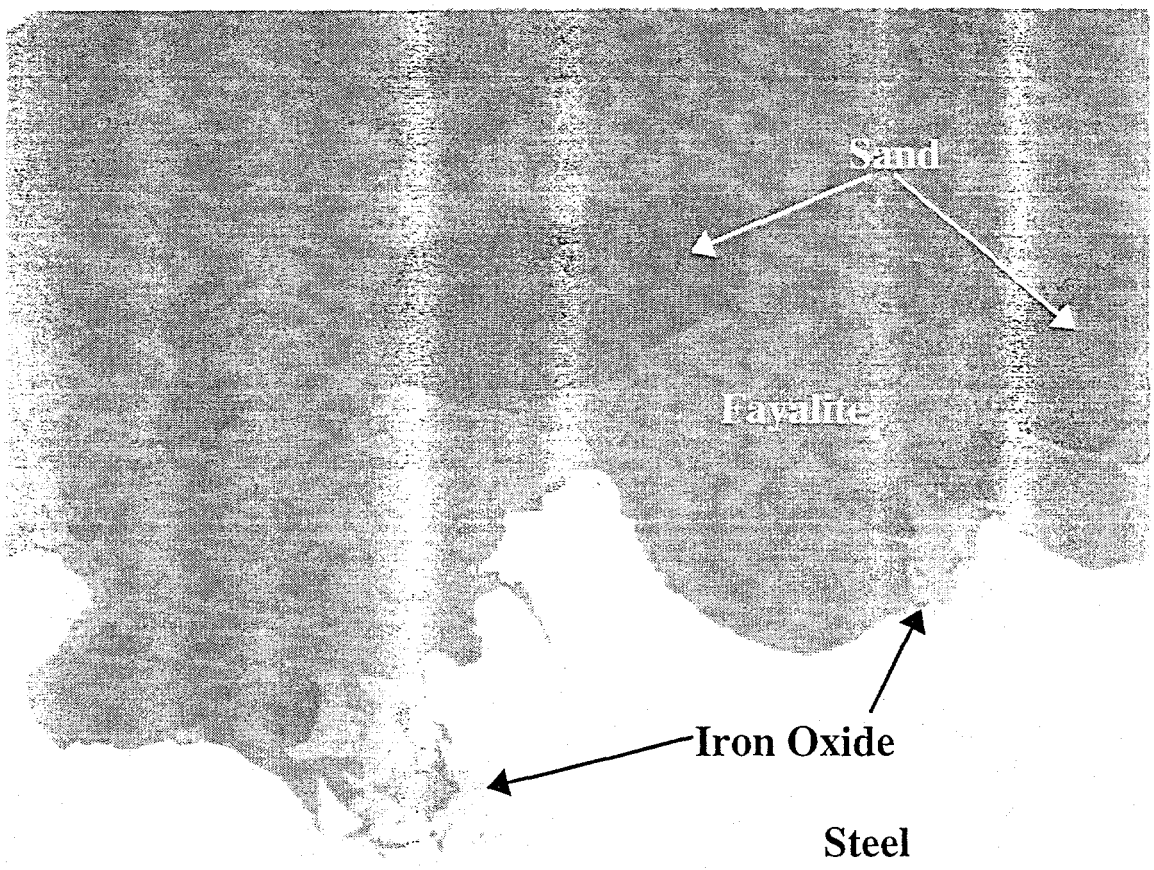

Figure 5-6. Photomicrograph of casting section from a green sand mold at 400 X, Experiment #14.

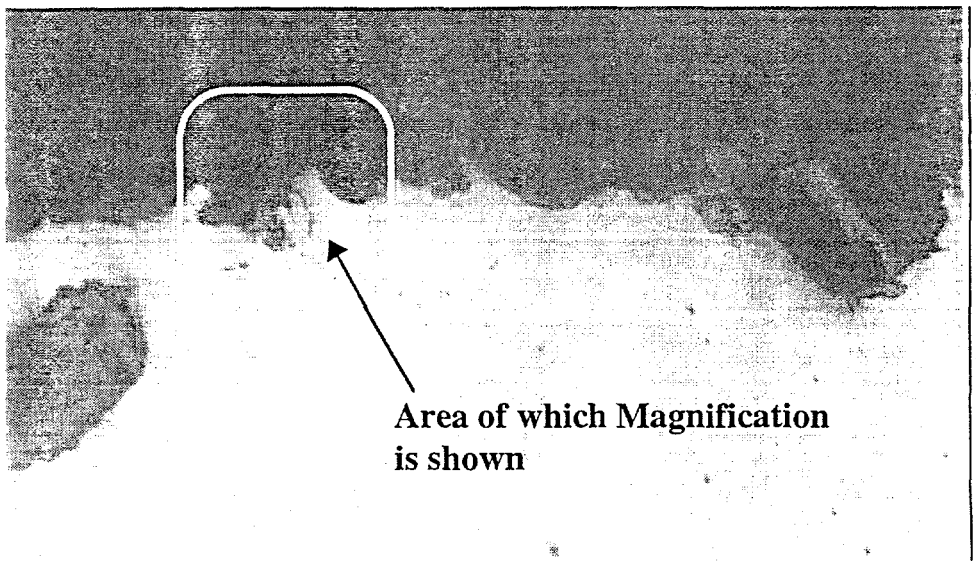

Figure 5-7. Photomicrograph of casting section from a green sand mold at 50 X, Experiment #14.

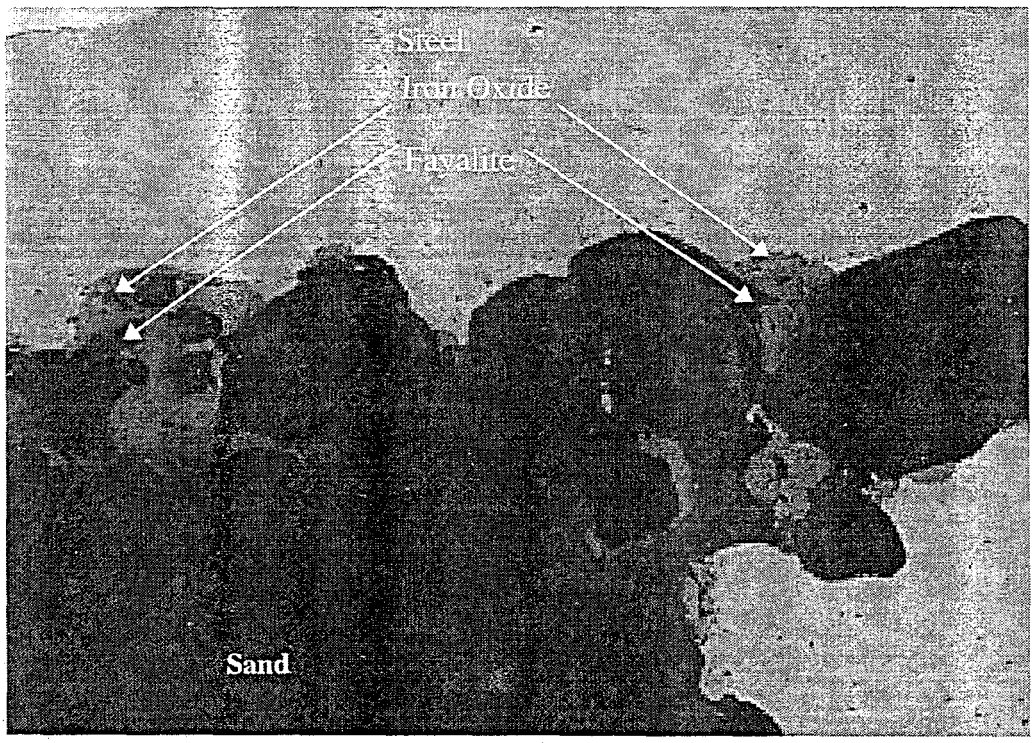

Figure 5-8. Photomicrograph of casting sections from a green sand mold, Experiment #18.

The data obtained from the green sand mold with no sea coal addition (Experiment 17) is shown in Figure 5-9. It differs from the other green sand mold data in three primary ways. First, it takes approximately one minute longer for the air to be flushed from the interface when no

carbon is present in the mold. This increased time is most likely due to oxidation reactions that produce low volume products, leaving the temperature increase as the only driving force for expansion. Reaction 5-3 produces essentially no increase in volume. It is also significant that the H_2 concentration increases nearly 30 seconds prior to increases in either CO or CO_2.

Reaction 5-3 $\quad Fe(l) + H_2O(g) \rightarrow FeO(l) + H_2(g)$

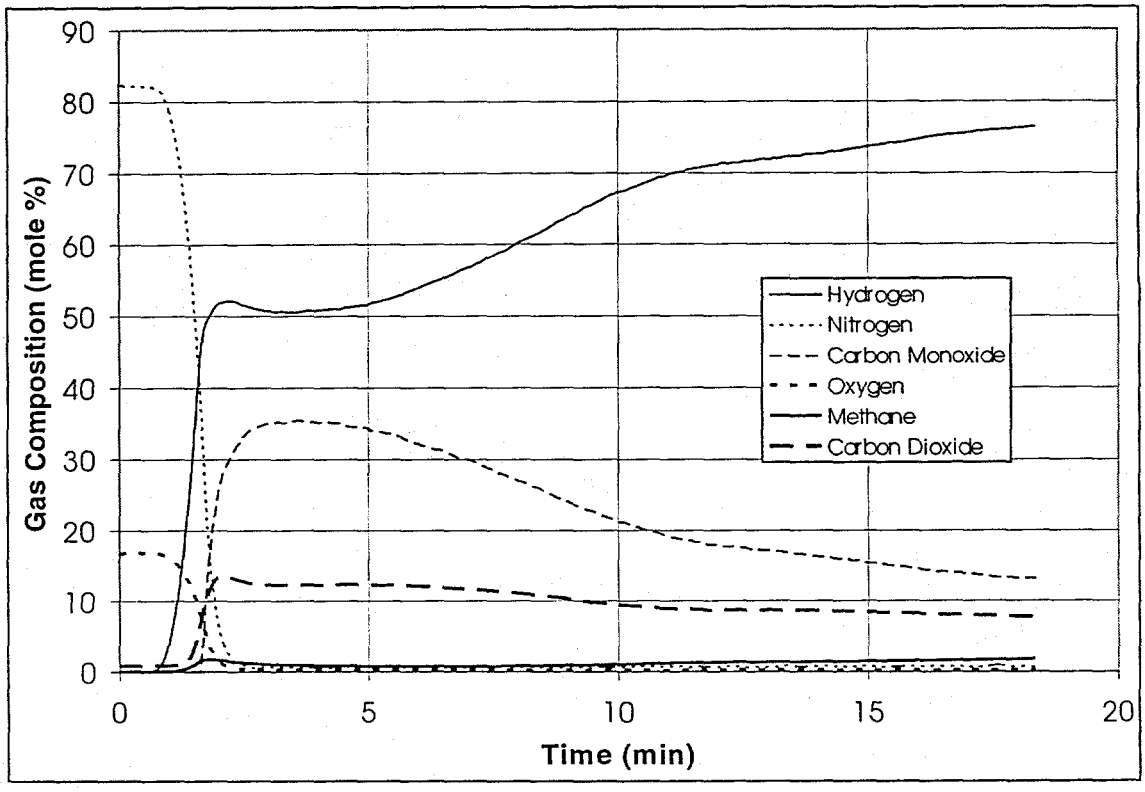

Figure 5-9. Gas composition for a green sand (no carbon) mold, Experiment #17.

The predominance of Reaction 6 at one minute into the run would explain why H_2 increases prior to CO and why more time is required to flush the mold. Unfortunately the production of FeO at this time cannot be verified. However, inspection of the casting upon cooling showed large quantities of fayalite which certainly indicates Reaction 6 is occurring. The photomicrograph of this casting section showing the presence of fayalite and iron oxide can be seen in Figure 5-10.

Secondly, the concentration of CO_2 is approximately 10% for most of the run with no carbon additions while it is only a few percent with the added C. This is also what would be expected when the concentration of C in the mold is reduced. When the quantity of water that is reacted is held constant and less C is provided, the quantity of CO produced goes down while that of CO_2 goes up. Third, the concentration of H_2 increases throughout the run while that of CO decreases. The O and H_2 contained in the gas phase species produced should be equal, unless some reaction products are either liquid or solid. Therefore the increasing H_2 concentration and decreasing CO concentration indicate that the oxygen from H_2O is oxidizing iron rather than C. Inspection after

cooling revealed a thick layer (1/8" or larger) that separated from most areas of the casting upon shake-out. Analysis of a section of this layer showed that it contained sand grains embedded in fayalite and iron oxide.

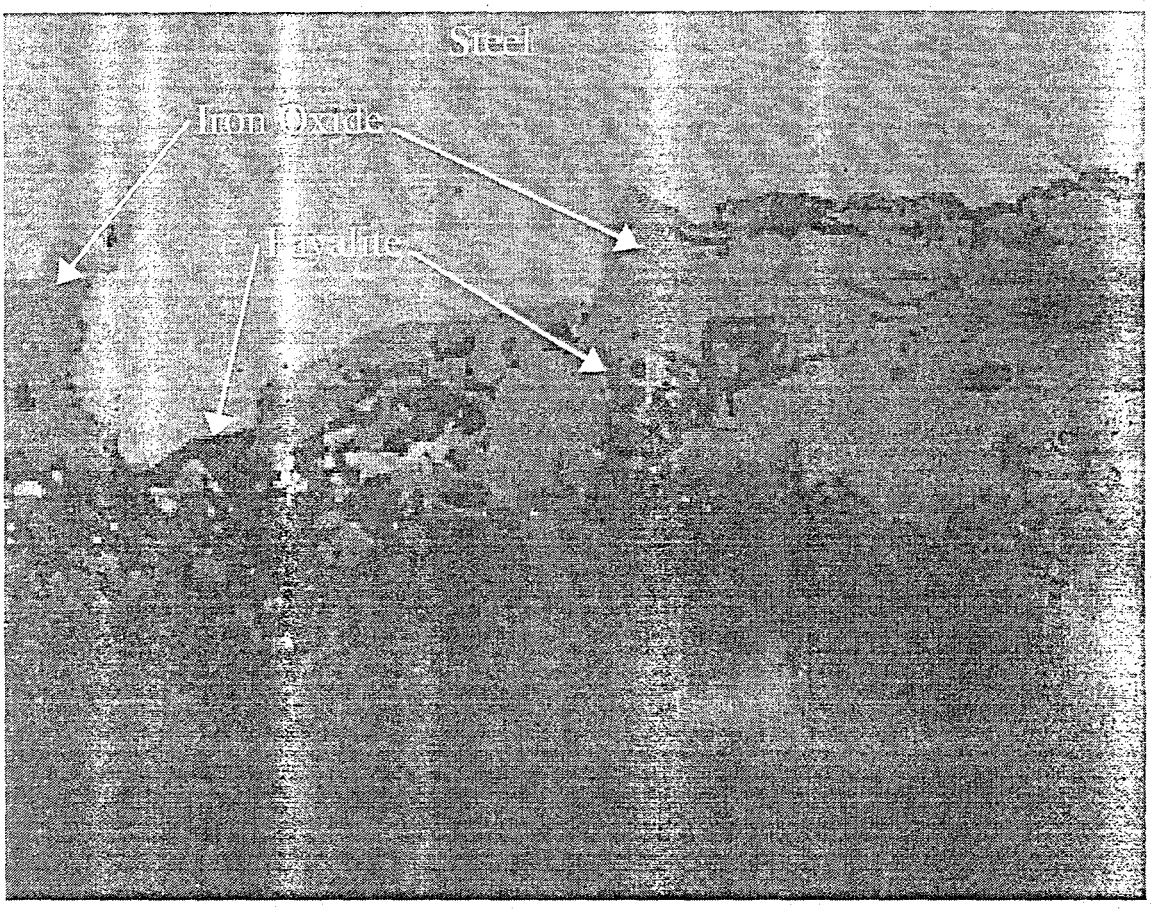

Figure 5-10. Photomicrograph of casting from green sand mold (no carbon), Experiment #17.

The effect of no carbon additions can best be seen by comparing the maximum CO_2/CO ratios. For the castings with carbon additions the highest values obtained were approximately 0.5, and 0.18 (Figure 5-4 and Figure 5-5) which are considerably lower than the value of 1.8 (Figure 5-11) obtained when no carbon was added to the mold.

Experiment 15 performed with a sodium silicate mold demonstrated that nearly six minutes was required to flush the air from the interface (Figure 5-12). This is primarily due to the lower concentration of water contained in sodium silicate molds, 2.5 percent, versus the 4 percent moisture contained in green sand. The concentration of hydrogen begins to increase one minute before that of CO_2 and two minutes before that of CO. This would indicate, as with the green sand no carbon mold, that oxidation of iron is taking place. Inspection of the casting revealed a layer that was attached but could be pried loose from the casting. The photomicrographs in Figure 13 and Figure 14 show the presence of fayalite in this layer as well as on the main casting.

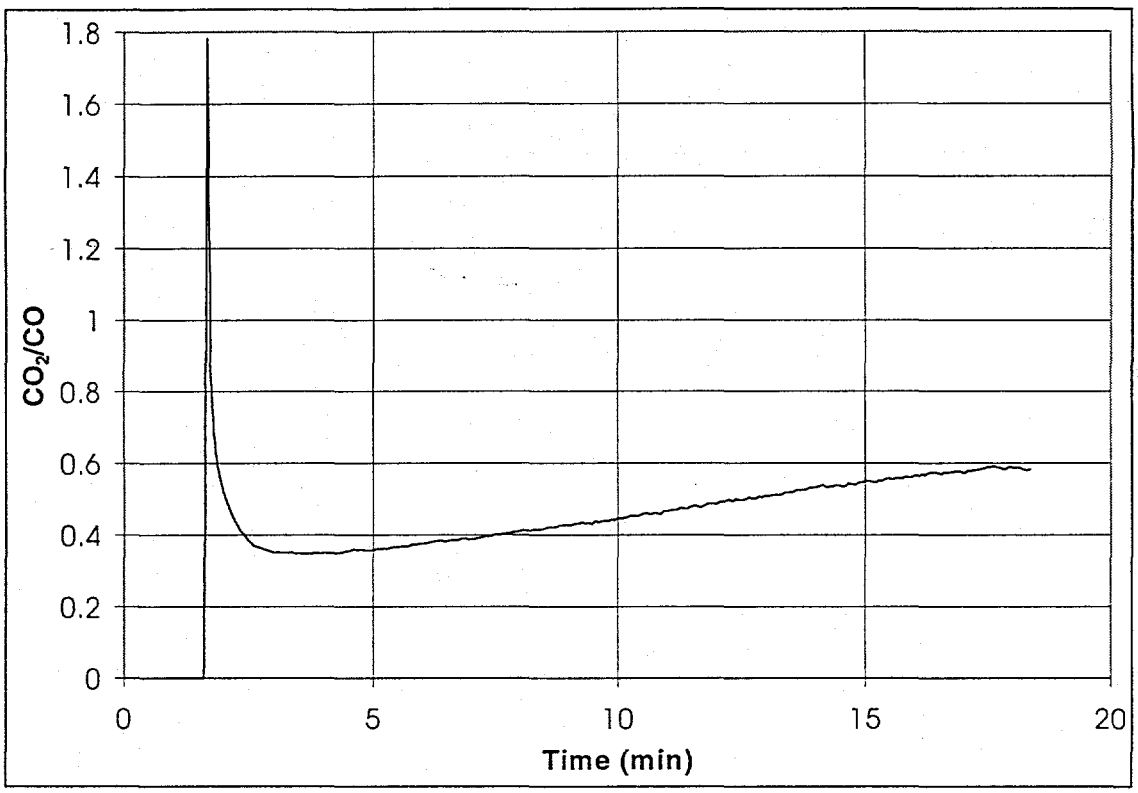

Figure 5-11. CO_2/CO for a green sand mold with no carbon, Experiment #17.

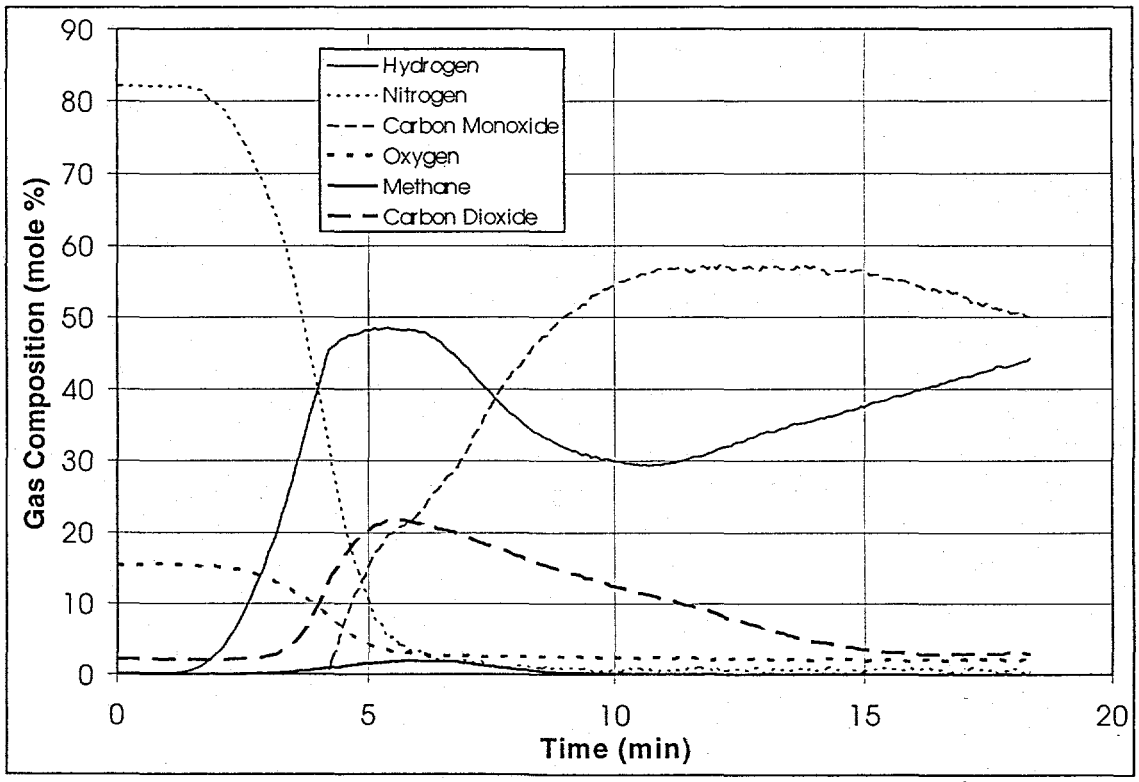

Figure 5-12. Gas composition for a sodium silicate mold, Experiment #15.

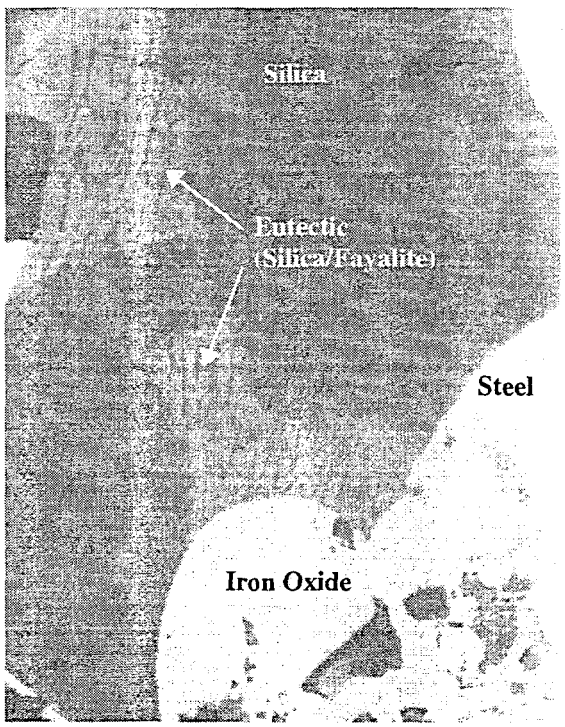

Figure 5-13. Photomicrograph of main casting section from a sodium silicate mold, Experiment #15.

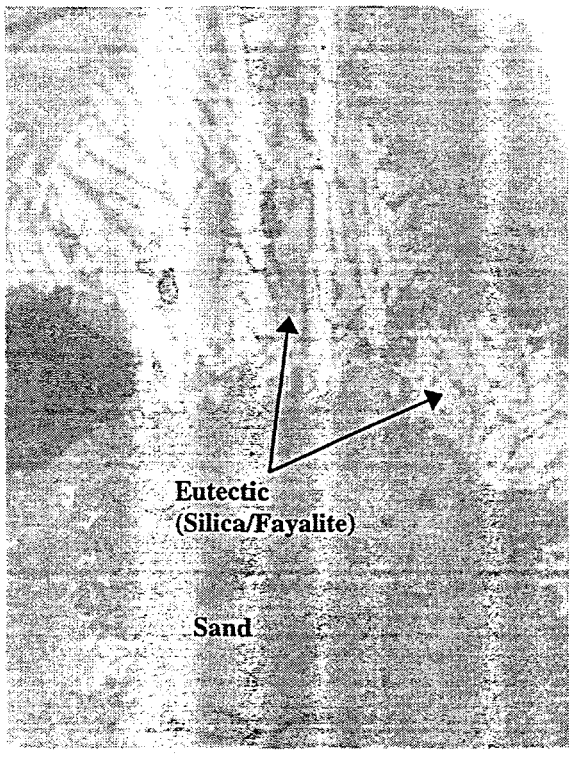

Figure 5-14. Photomicrograph of section from attached layer of a sodium silicate mold, Experiment #15.

Although the CO_2/CO ratio peaks at over sixty (Figure 5-15) the layer formed on this casting was not nearly as thick as that formed with the green sand no carbon mold. This, in conjunction with the fact that the CO concentration is greater than that of H_2 at times beyond eight minutes, suggest that some other reactions must be taking place. One possibility is that the highly oxidizing atmosphere at the beginning of the run oxidized iron beyond FeO to Fe_2O_3. The Fe_2O_3 could then be reduced to FeO after eight minutes into the run by carbon diffusing out of the bulk steel. This additional source of oxygen to produce CO would result in higher CO and lower H_2 concentrations as seen.

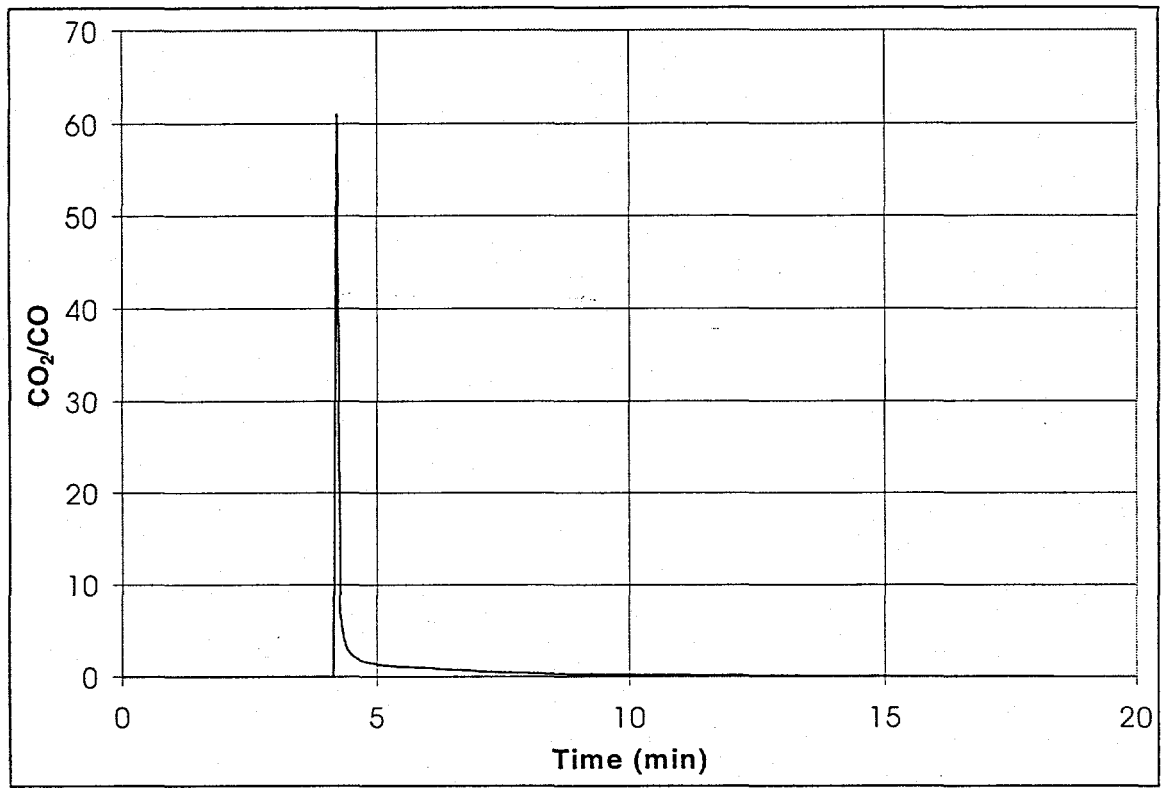

Figure 5-15. CO2/CO for a sodium silicate mold, Experiment #15.

The reduction of all Fe_2O_3 to FeO or Fe would cause the layer to be more firmly attached, as found with this casting, since oxide layers composed of a mixture separate more easily from iron because of the difference in coefficients of expansion. Studies on pinhole defects have shown that gray iron castings can absorb H_2 from the water contained in green sand molds and this would cause the lower concentrations of H_2 observed in this experiment.[39] However it is unlikely that this is occurring in this steel casting experiment because the H_2 concentration is decreasing after six minutes into the run. This is near the time at which the casting solidifies causing a marked decrease in H_2 solubility.

Experiments 1 and 16 were performed in resin bonded molds. Once again significant quantities of gas are produced; primarily H_2 and CO which flush air from the system rather quickly as seen in Figure 5-16 and Figure 5-17. The CO_2/CO ratios seen in Figure 5-18 and Figure 5-19 suggest that oxidation of iron should occur but no penetration was found on these castings. No definite explanation is available but two possibilities exist. First, the only moisture present in the resin bonded mold is that due to the humidity of the ambient air. This would eliminate the enlargement of pores caused by the dissolution of silica in steam.

Second, only the concentrations of the gases measured can be verified. There are certainly other gases present at the interface and one or more of them could be present in significant concentrations. If present at the interface another component could condense in the

sample lines or be absorbed by the calcium chloride in the drying tube. Thus an unknown vapor could provide a more reducing atmosphere at the interface yet remain unobserved.

A decrease in pore size would actually have two effects. The first is, of course, to increase the pressure required for penetration. The second would be to decrease the permeability of the mold at the interface. If lowered enough this would have the effect of sealing the surface of the casting from the gases present at the probe sight.

With the exception of Experiments 7 and 10 no penetration was seen with coated molds regardless of the properties of the mold or the coating. It is believed that penetration was caused in Experiments 7 and 10 by slag and a coating failure respectively. The castings produced in molds without coatings (Experiments 5, 9 and 11) all exhibited penetration. The action of these mold coatings may be similar to those of others studied earlier. Small particles of the coating decrease the pore size of the mold and may also expand when heated, further decreasing the ability of metal to penetrate the mold. The material may also be less wetting than the bulk mold material and be more resistant to attack by iron oxide. Most evidence suggests that coatings do reduce penetration, the primary problem being their proper application and the elimination of cracks which develop in the coatings.

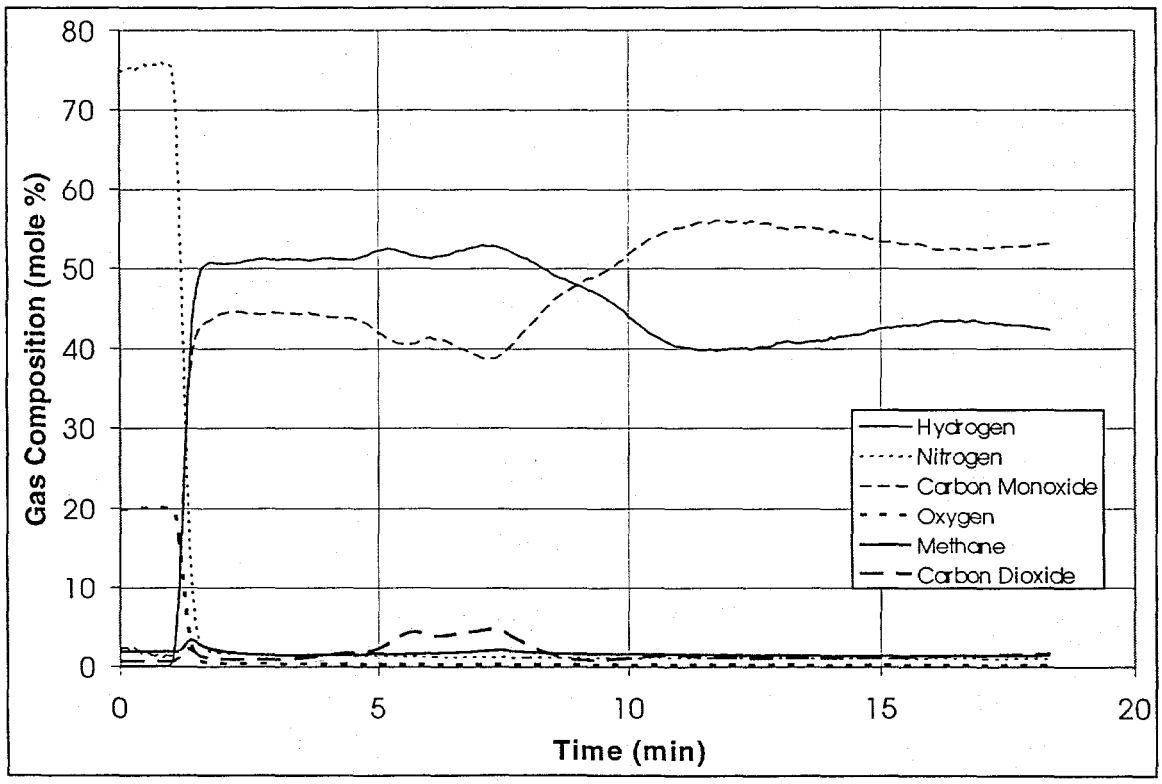

Figure 5-16. Gas composition for a resin bonded mold, Experiment#1.

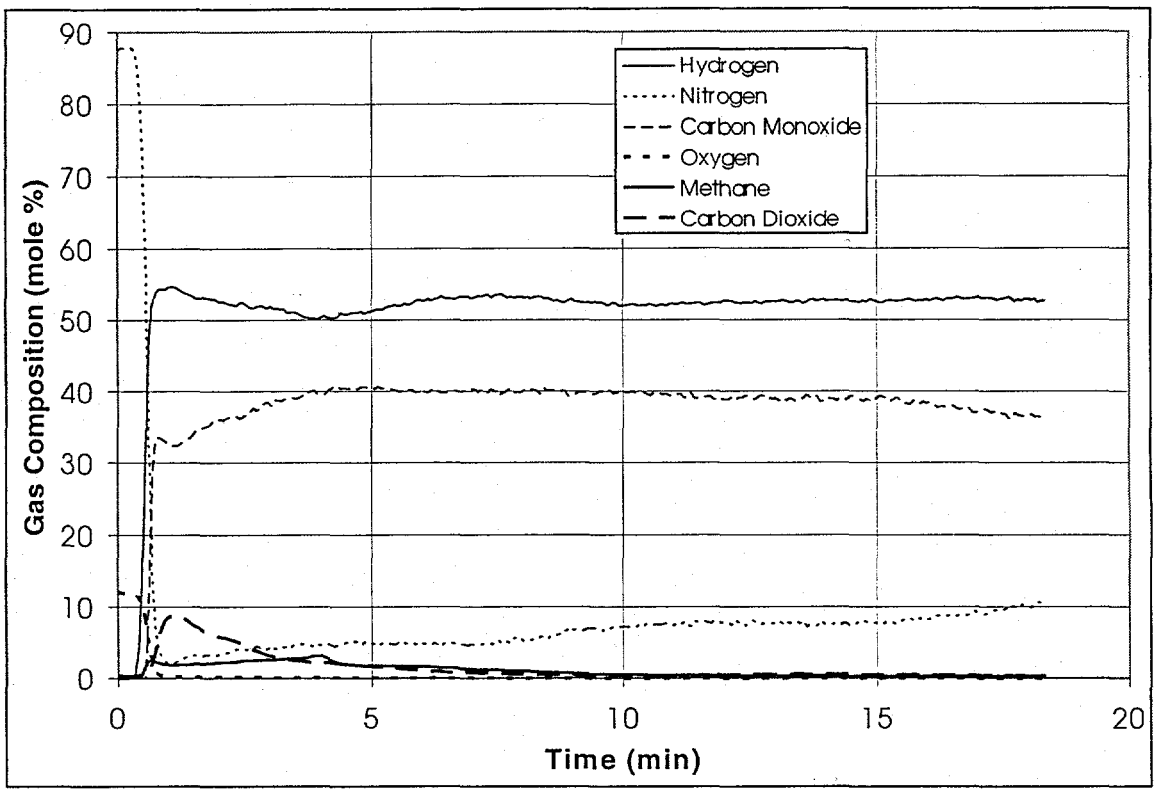

Figure 5-17. Gas composition for a resin bonded mold, Experiment #16.

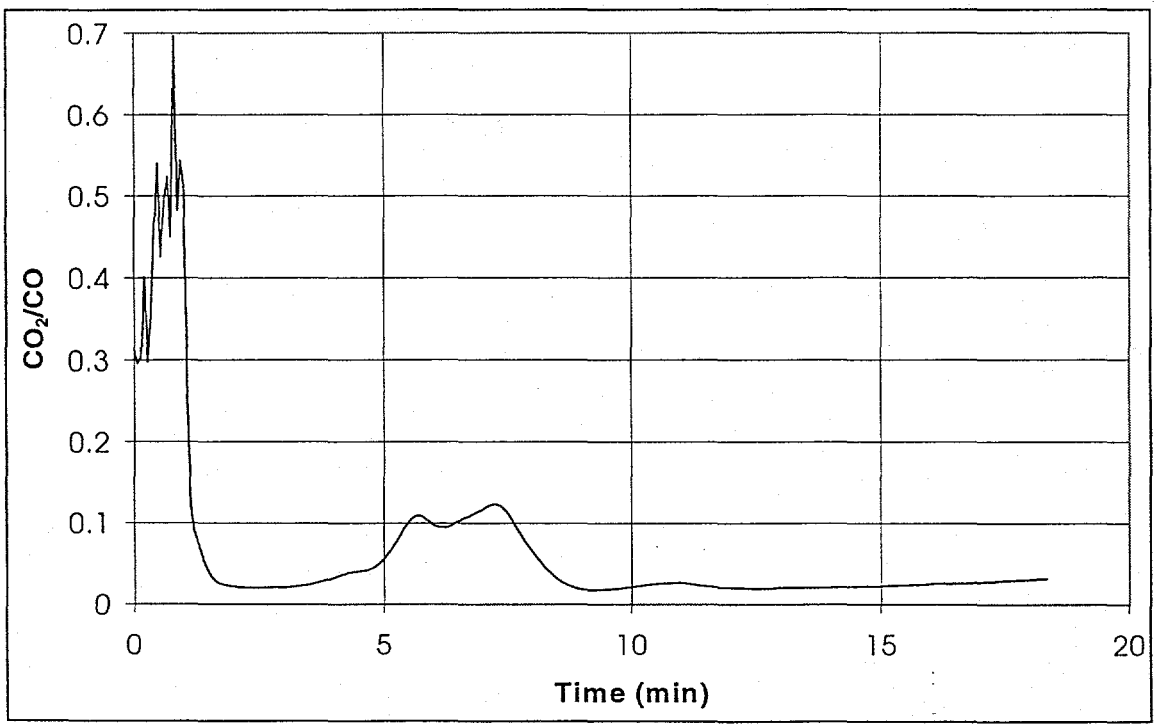

Figure 5-18. CO_2/CO for a resin bonded mold, Experiment #1.

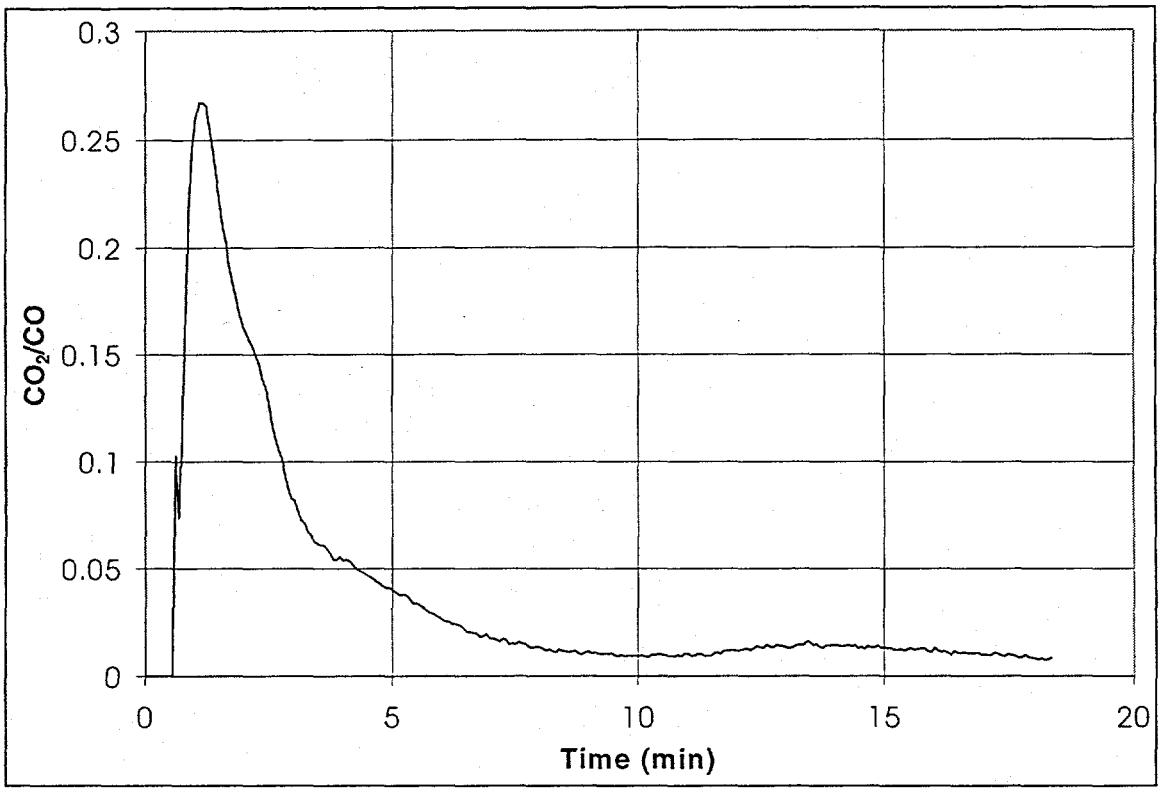

Figure 5-19. CO_2/CO for a resin bonded mold, Experiment #16.

5.3. Conclusions

Interfacial atmospheres are most oxidizing just after the casting is poured but may be capable of producing penetration well after the casting surface solidifies. The high initial oxidizing ability is due to the large amount of oxygen (primarily that contained in the condensed phase water) initially present in the mold. The rapid expansion of gases caused by reactions and temperature increase quickly blankets the casting surface with hydrogen and carbon monoxide. This protective layer of gases makes it more difficult for water to diffuse to the interface while carbon can diffuse at very near the initial rate. This causes the oxidizing ability of the atmosphere to decrease rapidly. When solid steel begins to form at the interface the ability of carbon to diffuse to the interface decreases markedly. This can cause a slight increase in oxidizing ability. This brings up the important question of weather penetration must occur while the steel is molten or if it can occur in the solid state. The question is investigated and answered in the following chapter.

Carbon additions to green sand molds are not able to eliminate chemical penetration with low carbon steels. A marked decrease is obtained in the oxidizing ability of the gases produced as well as a decrease in the severity of the penetration. The condensed phase moisture may simply contain too much oxygen to be totally consumed by the carbon at the interface. Higher carbon concentrations in the mold are not used because of their diffusion into the steel causing carburization.

Mold coatings can eliminate chemical penetration if proper application is achieved. There are several ways in which coatings work. Their smaller particle size makes it more difficult for steel to enter the mold pores. Their composition may increase the contact angle. Some materials also tend to expand when heated. This increases their ability to decrease the diffusivity of gases at the interface. Therefore even if oxidizing gases are present in the mold they cannot oxidize the steel because they cannot get to it and penetration is prevented. The primary problems with mold coatings is the difficulty in achieving proper application.

6. Solid State Kinetic Studies

One of the primary questions concerning chemical penetration is when it takes place. Oxidation of iron at the mold-metal interface may increase the contact angle enough for the molten steel to flow between the sand grains before solidification occurs. The steel may solidify before penetration occurs but iron oxide and fayalite, having a lower melting temperature, may still penetrate the mold. In addition, a combination of both scenarios may occur, penetration of molten steel at early times followed by the formation of additional iron oxide and fayalite after solidification of the steel.

6.1. Solid State Reactions Between Sand and Steel

To determine if penetration may occur while the metal is in the solid state, a series of experiments were carried out in a tube furnace. Two different samples of steel were used for this experiment, their compositions are given in Table 6-1. The composition of sample A was chosen because it approximates that used in the castings prepared at The University of Alabama, sample B was studied because of its high Mn concentration which is known to increase penetration. Steel samples were cut into 5/16" square blocks with one 1/8" diameter hole drilled 1/8" deep into the top as shown in Figure 6-1. Diagram of cubic steel samples used for kinetic studies.. This cavity was filled with sand to simulate the sand to metal contact present in a steel casting after metal solidification. The samples were then heated in a tube

Table 6-1. Composition of Steel Samples.

Sample	C	Mn	Si	Cr	P	Al
A	0.30	0.77	0.41	0.575	0.008	0.033
B	1.15	13.96	0.82	0.030	0.035	0.044

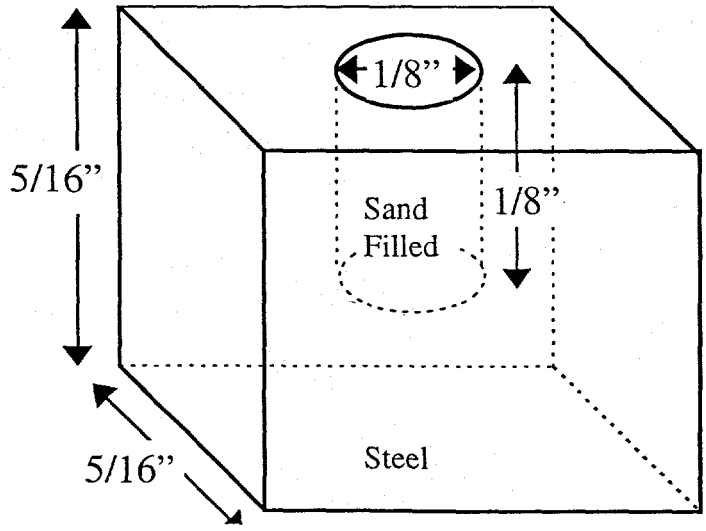

Figure 6-1. Diagram of cubic steel samples used for kinetic studies.

furnace under an argon atmosphere. After reaching the desired temperature the furnace was purged with either pure CO_2 or a mixture of CO_2 and CO. After heating for a set period of time the furnace was turned off and purged with argon.

After cooling the samples were inspected visually for the presence of oxidation products and the attachment of sand. Results varied widely even when all known variables were held constant as shown in Table 6-2. Many of samples were studied more thoroughly with a Scanning Electron Microscope (SEM) as well as an optical

Table 6-2. Physical Appearance of Solid State Penetration Samples.

#	Sample	Temp. °F	Time Min.	Appearance
13	A	1400	15	clean
14	A	1400	15	little oxidation
16	A	1300	15	some attached sand
17	A	1300	30	clean
18	A	1400	15	little oxidation
19	A	1432	30	very clean
20	A	1300	30	relatively clean
29	A	1300	60	little sand but well attached
30	A	1200	60	well attached sand
31	A	1300	60	well attached sand
32	A	1432	60	well attached sand
33	A	1200	60	well attached sand
34	A	1200	60	well attached sand
35	A	1200	60	attached sand but little oxidation
36	A	1300	60	attached sand but little oxidation
37	A	1432	60	clean on 70% of surface, sand attached to 30 %
38	B	1200	60	significant attached sand
40	A	1200	60	attached sand
41	A	1200	60	sand is not as dark as usual
43	A	1300	30	attached sand and oxidation
44	A	1300	30	attached sand and oxidation
45	A	1300	30	attached sand and oxidation
46	A	1300	30	attached sand and oxidation
47	A	1300	30	attached sand and oxidation
52	A	1200	30	attached sand and oxidation
53	A	1432	60	attached sand and oxidation
54	A	1200	60	clean
55	B	1200	60	hole filled with oxidation products
56	A	1300	60	attached sand, significant oxidation
57	A	1432	60	some attached sand, little oxidation
58	B	1200	60	some oxide and attached sand grains
59	B	1432	60	attached sand grains appear molten
60	B	1300	60	dark surface but little oxidation product
61	A	1300	60	half clean, half oxidized

microscope. To do this the top surface of the samples were first ground away and polished. The instruments were then used to inspect the sample and look at iron oxide and fayalite that were produced in the experiment. It was found that fayalite could be produced not only on the inner

surface in contact with the sand (Figure 6-2), but also on the outer surface that is exposed only to CO_2 (Figure 6-3). In the latter case the silica required for fayalite formation is actually provided by the small concentrations contained in the steel. Because the physical appearance of the samples varied widely it was impossible to determine any significant difference in the results between the two sample types. However it was found in all cases that the fayalite could be easily removed. Thus while solid state reactions may affect the dimensions or decarburization of the casting, the products do not require expensive machining operations but can be easily removed by sandblasting.

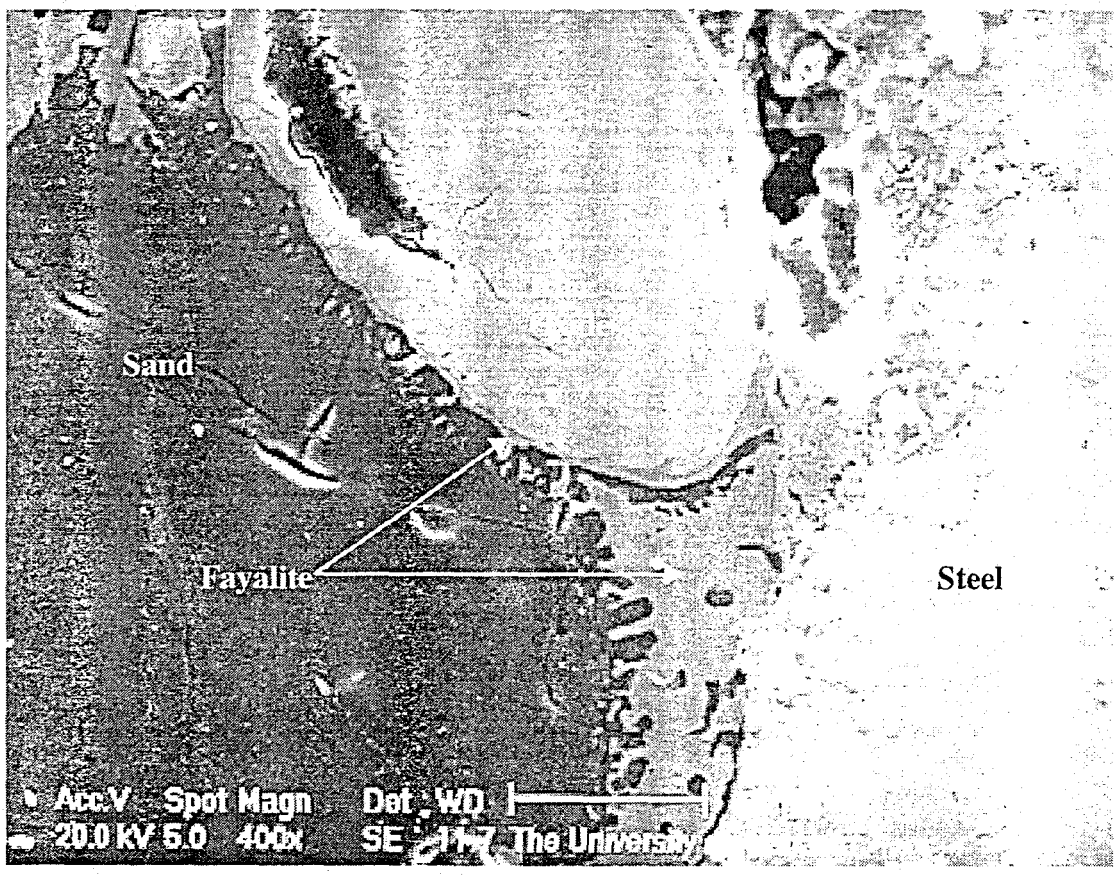

Figure 6-2. Photomicrograph of inner surface of kinetic sample.

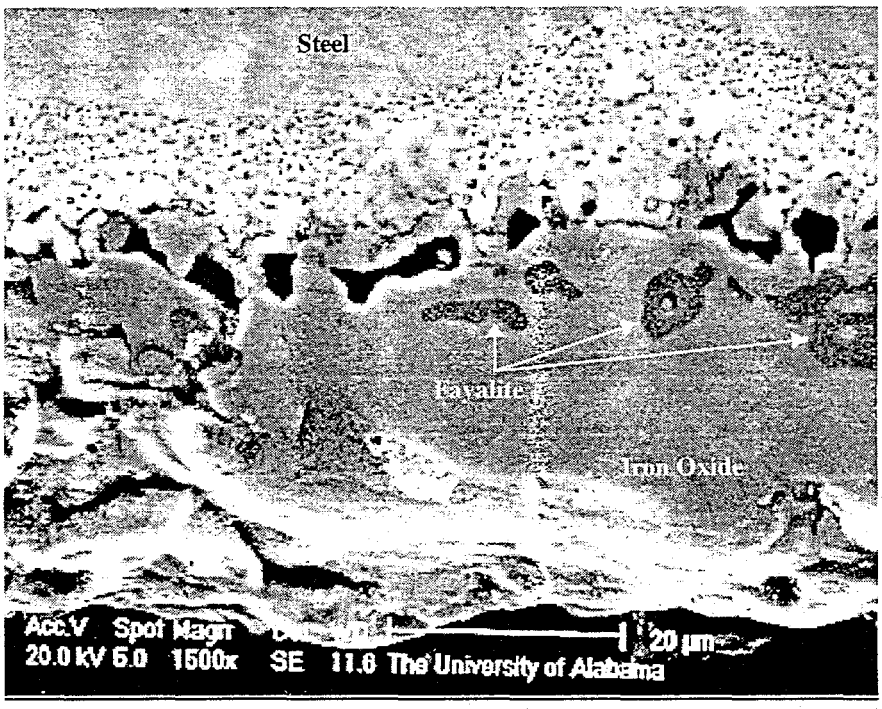

Figure 6-3. Photomicrograph of outer surface of kinetic sample.

Attempts were also made to determine the effect of heating time on decarburization as well as the change in carbon concentration with depth from the sample surface. This was done by etching the sample with Nital after polishing. The pearlite which contains higher concentrations of carbon then shows up as darker areas with the remaining steel forming a very light background, as shown in the middle of Figure 6-4. The dark areas at the top of the figure are due to iron oxide, the black areas indicate pores and crevices. In the dark semi-circle at the bottom of the figure can be seen individual sand grains embedded in mounting material.

Figure 6-4. Photomicrograph of kinetic sample etched with nital.

6.2. *Diffusion of Carbon Through Solid State Steel*

A second question is whether the oxidation of carbon contained in the steel is limited by the reaction rate at the steel surface or the rate of carbon diffusion through the steel to the surface. To answer this a 1/2" diameter 10-18 cold rolled steel rod was cut into 3" lengths as shown in Figure 6-5. The steel cylinders were heated in the tube furnace to the desired temperature under argon before being exposed to an atmosphere of CO_2. After a designated period of time the furnace was turned off and purged with argon. When cool the cylinders were sectioned across the diameter, polished, and etched with four percent nital. The cross sections were then viewed with an optical microscope to determine the percent pearlite. This can then be correlated to the percent carbon. Measurements were made of 225 square micron areas at 1/64" intervals across the diameter of the sample as shown in Figure 6-6. Even when two measurements are averaged there is a significant error in measurement. This can best be seen by viewing the data obtained for the blank sample.

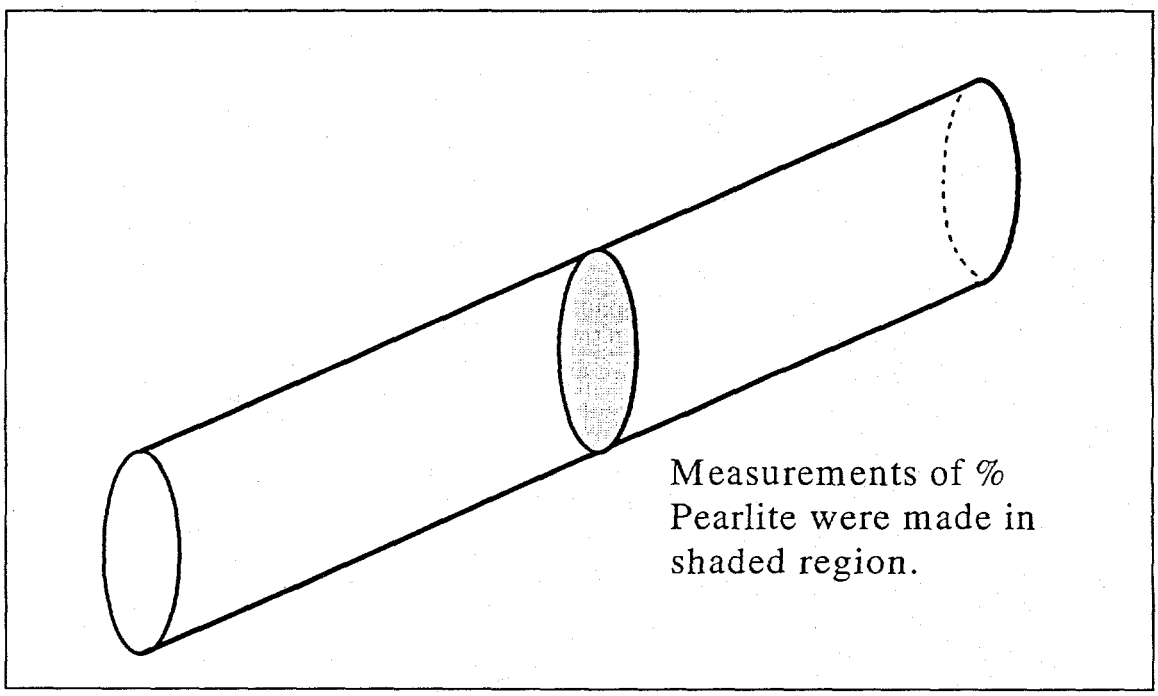

Figure 6-5. Diagram of cylindrical steel samples used in kinetic studies.

The mathematics of diffusion in a cylinder are well discussed by Crank.[40] If the assumption is made that diffusion of carbon is the limiting step then the following equation can be applied to find the experimentally determined diffusivity:

$$\frac{C - C_i}{C_0 - C_i} = 1 - \left(\frac{2}{a}\right)\sum_1^{\infty} \frac{\exp(-D\alpha_n^2 t) J_0(r\alpha_n)}{\alpha_n J_1(a\alpha_n)} \qquad (7.1)$$

where C is the concentration at radius r, C_i is the initial concentration, C_0 is the concentration at the surface and is assumed to be zero, a is the radius of the sample, D is the diffusivity of carbon through steel, α_n is the n^{th} root of $J_0(a\alpha_n) = 0$, J is the Bessel function, and r is the radius at the measured concentration. The summation above was truncated to the first four terms as additional terms have negligible value. The diffusivity was found by minimizing the sum of the squares of the deviations in D for each sample.

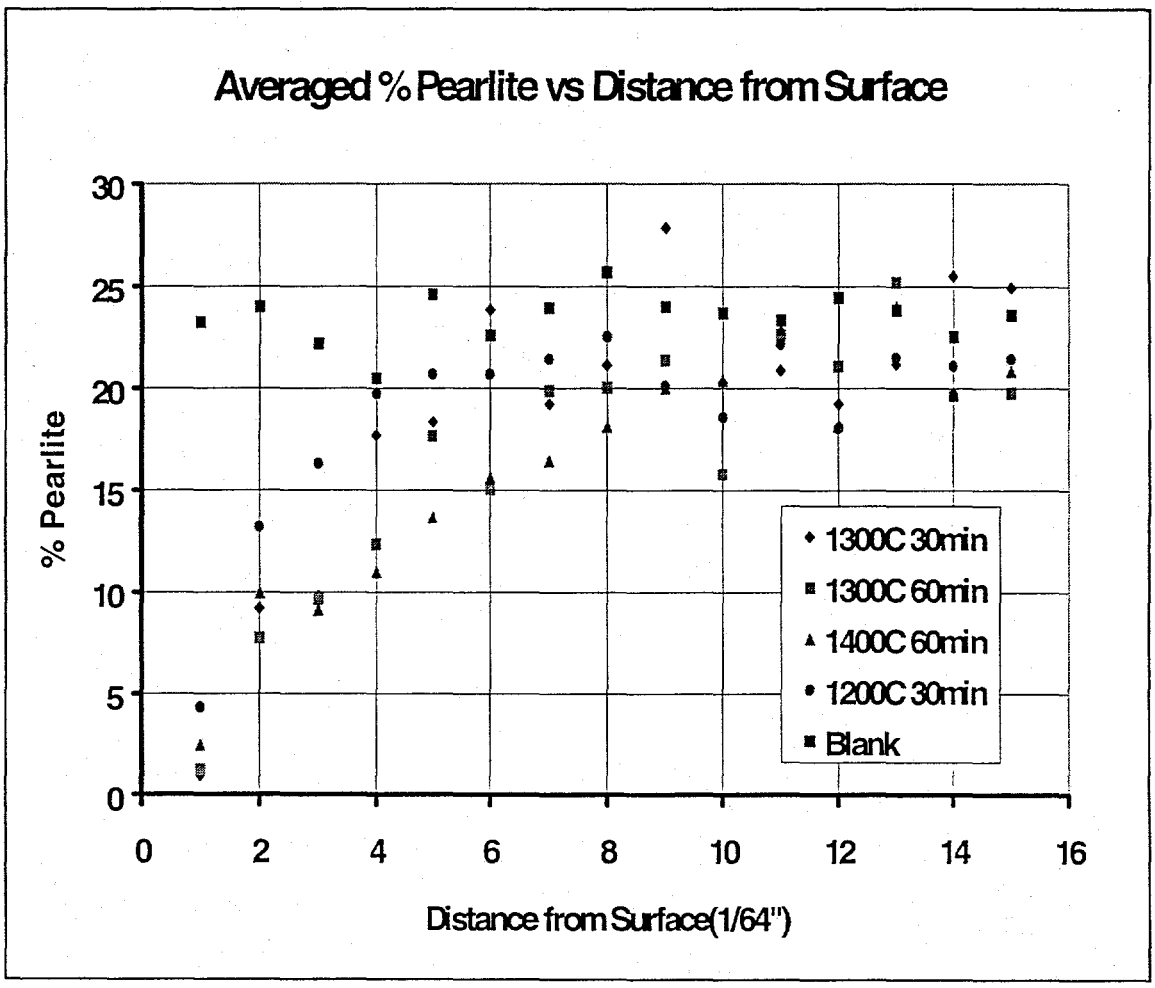

Figure 6-6. Averaged % pearlite as a function of depth.

The calculated diffusivity was found from

$$D = (7E-6)\exp\left[\frac{-31350}{RT}\right] \qquad (7.2)$$

where D is the diffusivity (m^2/s), R is the Ideal Gas Constant (1.987cal/mol-K), and T is the Temperature (K).[41] The calculated and experimentally determined diffusivities are compared in Table 6-3. For each sample the experimental value is either equal to or greater than the calculated

diffusivity. Thus the initial assumption, that the reaction is diffusion rate limited, appears to be correct.

Table 6-3. Calculated and Experimentally Determined Diffusivities.

T(C)	Time(min)	Experimental D (m^2/s)	Calculated D (m^2/s)
1200	30	2.5E-10	1.6E-10
1300	30	4.6E-10	3.1E-10
1300	60	4.4E-10	3.1E-10
1400	60	5.6E-10	5.6E-10

6.3. Conclusions

Penetration can occur after solidification. This is significant because of the low diffusivity of carbon through solidified steel. Although the flux of water to the interface also decreases with time it can still be greater than that of carbon. Large castings may be able to continue producing fayalite and iron oxide for long periods of time after solidification has occurred. Thus the rate of formation is low but total fayalite production may be high.

Fortunately, penetration produced after solidification is easily removed. This would seem to explain some foundrymen's experience that fayalite actually aids in shake out. The penetration they are experiencing is apparently produced after solidification. However, penetration that is produced while the casting surface is molten can be very difficult to remove. This would suggest that fayalite does not physically adhere to the casting. The removal problem may only be produced when steel penetrates into the pores of the mold. It can also be argued that true penetration only occurs when molten iron penetrates the mold, not its oxidation products.

The kinetic studies suggest that the rate of oxidation of carbon at the solid steel surface is diffusion rate limited (at least down to 1200 C the lowest temperature investigated). As stated earlier, this means that very large castings may continue to be oxidized for long periods of time.

7. Model for Chemical Penetration

7.1. Elements of the Chemical Penetration Model

Unless carbon is abundant in the mold, the formation of carbon monoxide and a reducing layer of gas in the mold will depend on the reaction of water vapor with the carbon dissolved in the steel. Penetration by reaction with gas occurs when the carbon from the steel is oxidized by the gases from the mold to a point where carbon can no longer protect the iron from oxidizing.

To explain this mathematically, three different quantities need to be expressed. First, the minimum carbon content (or critical carbon) at the interface required to prevent the oxidation of the iron. It can be calculated using a thermodynamic approximation. Second, the amount of carbon diffusing to the mold/metal interface needs to be determined. Finally, the flux of water vapor (oxygen) through the mold to the interface needs to be calculated. Three separate models were developed to accomplish these goals. These are discussed in detail in the following sections.

7.2. Thermodynamic Model for Evaluation of the Critical Carbon Content

An equilibrium may be written between the measurable quantities in the mold atmosphere and the main constituents of the alloy composition, as follows:

$$2Fe + \frac{3}{2}CO_2 \rightarrow 2FeO + CO + \frac{1}{2}\underline{C} \qquad \text{(Reaction 7.1)}$$

Assuming that iron and iron oxide are pure phases (*i.e.* activity is equal to unity), the equilibrium constant, k_{eq}, of this reaction is:

$$k_{eq} = \frac{p_{CO} \cdot \underline{C}^{0.5}}{p_{CO_2}^{1.5}} = \exp\left(\frac{-\Delta G}{R \cdot T}\right) \qquad (7.1)$$

where, p is the respective partial pressures of the subscript gases in atmosphere, ΔG is the free energy in J/mol, and R is the ideal gas constant 8.314 J/(mol·°K), and the units of $\underline{C}$ are weight percent, Fe and FeO are solid or liquid, CO and CO_2 are gases and $\underline{C}$ is the amount of carbon dissolved in the steel. Equation 7.1 may then be evaluated at various temperatures, solved for the critical carbon content, C_{cr}, and fit to an exponential function of temperature to give:

$$C_{cr} = \frac{p_{CO_2}^3}{p_{CO}^2} 0.1 \cdot \exp(0.002 \cdot T) \qquad (7.2)$$

It remains now to calculate the carbon diffusion to the interface.

7.3. Model for Carbon Diffusion to the Interface

7.3.1. Computational details

The governing equations for heat transfer and diffusivity are both partial differential equations (PDE). The PDE for heat transfer is:

$$\frac{\partial T}{\partial t} = \alpha \frac{\partial^2 T}{\partial^2 x} + \frac{\Delta H_f}{C_p} \frac{\partial f_s}{\partial t} \tag{7.3}$$

where, T is the temperature in °C, t is the time in seconds, α is the thermal diffusivity in m^2/s, x is the distance in m, ΔH_f is the heat of fusion in J/kg, C_p is the specific heat in J/kg·K, and f_s is the fraction of solid.

The PDE for diffusion is very similar to Equation 7.3 except that solutal diffusivity replaces thermal diffusivity, and there is no source term; the equation is:

$$\frac{\partial C}{\partial t} = D \frac{\partial^2 C}{\partial^2 x} \tag{7.4}$$

where, C is the composition in weight percent and D is the solutal diffusivity in m^2/s.
The fraction of solid is assumed to be determined by a linear function

$$f_S = 1 - \left(\frac{T - T_S}{T_L - T_S} \right) \tag{7.5}$$

where, T_s is the solidus temperature, T_L is the liquidus temperature, and k is the partition coefficient.

The discretized form of Equation 7.3 with no latent heat for an interior node or an exterior node with a constant boundary condition and an exterior node with a flux boundary condition are given in below. A schematic of the grid is given in Figure 7.1.

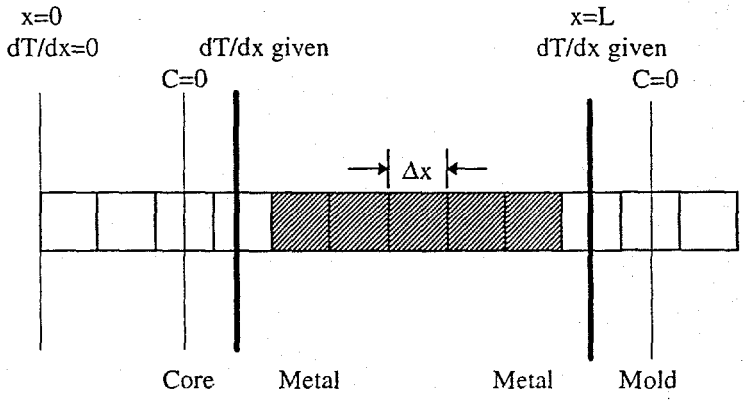

Figure 7-1. Drawing of grid system and boundary conditions used in the program.

Constant boundary condition

$$T_i^{n+1} = F_0\left(T_{i-1}^n + T_{i+1}^n\right) + \left(1 - 2 \cdot F_0\right)T_i^n \tag{7.6}$$

where, i is a subscript for x-space, n is a superscript for time, F_0 is the Fourier number ($\alpha \cdot \Delta t/\Delta x^2$).

Flux boundary condition

$$T_i^{n+1} = 2 \cdot F_0\left(T_{i+1}^n + \frac{h \cdot \Delta x}{k} T_\infty\right) + \left(1 - 2 \cdot F_0\left(\frac{h \cdot \Delta x}{k} + 1\right)\right)T_i^n \tag{7.7}$$

where, h is the heat transfer coefficient in W/(m^2·K), k is the thermal conductivity in W/(m·K), Δt is the time step in s, and Δx is the grid spacing in m..

An interior node with latent heat is as follows:

$$T_i^{n+1} = F_0\left(T_{i-1}^n + T_{i+1}^n\right) + \left(1 - 2 \cdot F_0\right)T_i^n + \frac{\Delta H_f}{C_p} \cdot df_s \tag{7.8}$$

where, df_s is the change in the fraction of solid.

The discretization of Equation 5.4 is:

for interior nodes

$$C_i^{n+1} = F_0\left(C_{i-1}^n + C_{i+1}^n\right) + \left(1 - 2 \cdot F_0\right)C_i^n \tag{7.9}$$

for exterior nodes

$$C_i^{n+1} = 2 \cdot F_0\left(C_{i-1}^n\right) + \left(1 - 2 \cdot F_0\right)C_i^n \tag{7.10}$$

Table 7-1. Boundary conditions used for model.

Variable	Variable value	X position
∂T/∂x	0	0
∂T/∂x	flux based on heat transfer coefficient	core/metal interface
∂T/∂x	flux based on heat transfer coefficient	L
C	0	core/metal interface -1
C	0	L + 1

The boundary conditions to be used are shown in Fig. 7-1 and listed in Table 7-1. The boundary conditions for the heat flow are a zero heat flux at x=0 and a heat flux at x=L. There is also an air gap at the interface which uses the same heat transfer coefficient as that for the outside

boundary. The initial conditions are that all temperatures equal the pouring temperature for the casting, and temperatures in the core are at the ambient temperature. The boundary conditions for the diffusion are at x=interface-1: C=0 and at x=L+1: C is also equal to zero. The initial condition for the diffusion is that all compositions are equal to the initial composition.

For the explicit scheme used to be stable the Fourier number must be less than 0.5; however, this is without the latent heat term which necessitates a much smaller time step. The scheme used is explicit forward in time and central in space differencing. This scheme is first order accurate in time and second order accurate in space.

7.4. Model for Water Vapor (Oxygen) Flux

The mold is modeled as though consisting of three different regions, each with one or more moving boundaries. Beginning at the metal interface and extending some distance away is the dry sand zone as shown in Figure 7-2. In this region the only moisture present is in the vapor phase. Heat is transferred from the casting to the mold at the interface, causing the temperature of the dry sand zone to increase with time. Of course, the temperature of this zone is highest at the metal interface and decreases with distance until the condensation temperature of water is reached. The point at which this temperature is reached is the forward boundary of the dry sand zone. As heat is conducted to the boundary water is vaporized, causing the boundary to move forward. The forward boundary of the dry sand zone is the rear boundary of the vapor transport zone. As water is being vaporized at the rear boundary of the transport zone it is being condensed at the forward edge. Thus both boundaries move with time, but not necessarily at the same rate. The temperature of this region remains constant at the condensation temperature of water.

Finally, the undisturbed region extends from the forward boundary of the vapor transport zone to the edge of the mold. The temperature of this region remains constant at the ambient. In reality there is no discontinuity in temperature at the forward boundary of the vapor transport zone. However, since the difference between ambient temperature and the boiling point of water is not large, the approximation is reasonable.

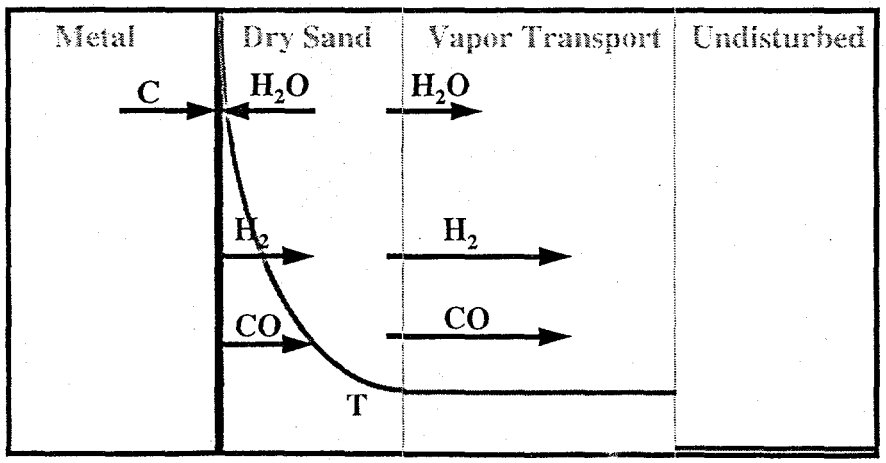

Figure 7-2. Flux and temperature profile of a sand mold.

7.4.1. Temperature Profile and Boundary Movement Equations

The equations given below for the movement of different zones through the mold are adapted from those by Tsai.[42] This model uses a heat transfer coefficient at the mold metal interface rather than set the temperature of the first node of the mold equal to that of the metal. Equations related to energy balances can also be found in the literature.[43] Beginning with an energy balance at the metal interface the stored energy can be expressed as:

$$E_{in} + E_{generated} = E_{stored} \tag{7.11}$$

Substituting for each of these terms we have:

$$E_{in} = hA(T_\infty - T_0) + kA(\partial T/\partial Z) \tag{7.12}$$

where h is a heat transfer coefficient (W/m^2K) between the molten metal and the sand, T_∞ is the temperature of the molten metal, T_0 is the temperature of the sand at the interface, k is the thermal conductivity of the sand (W/mK), A is the cross section area (m^2), Z is distance perpendicular to the metal surface (m), and T is temperature in the mold (K).

$$E_{generated} = 0 \tag{7.13}$$

$$E_{stored} = \rho C_d A(\Delta Z)(\partial T/\partial t) \tag{7.14}$$

where ρ is the density of dry sand (kg/m^3), C_d is the heat capacity of dry sand (J/kgK), and t is time (s). Substituting Equations 5.12-5.14 into equation 5.11 yields

$$hA(T_\infty - T_0) + kA(\partial T/\partial Z) = \rho C_d A(\Delta Z)(\partial T/\partial t) \tag{7.15}$$

At interior nodes of the dry sand region we have

$$\partial T/\partial t = \alpha(\partial^2 T/\partial Z^2) \tag{7.16}$$

where

$$\alpha = k/\rho C_d \tag{7.17}$$

At the interface of the dry sand and vapor transport zones the energy transported to the boundary must be equal to energy used in the vaporization of water. Therefore

$$k(\partial T/\partial Z) = -L\rho W(\partial \varepsilon_l/\partial t) \tag{7.18}$$

where L is the latent heat of vaporization of water (J/kg), W is the weight fraction of water in the vapor transport zone, and ε_l is the position of the dry sand front (m). At the forward edge of the

transport zone the energy provided by the condensation of water is used to heat the mold to the vaporization temperature. This yields

$$W = (W_0C_w + (1-W_0)C_d)(T_c-T^0)/L + W_0 \quad (7.19)$$

where W_0 is the initial weight fraction water, C_w is the specific heat of water (J/kgK), T_c is the vaporization temperature of water (K), and T^0 is the initial mold temperature.
Moisture removed to produce additional space in the dry sand zone must be equivalent to that added to the transport zone. Therefore

$$\int_0^t WV_1dt = \int_0^t (W - W_0)V_3dt \quad (7.20)$$

where V_1 is the moving speed of the vaporization interface and V_3 is the speed of the condensation interface. This yields

$$\varepsilon_3 = \varepsilon_1 W/(W-W_0) \quad (7.21)$$

where ε_3 is the position of the condensation front.
The energy transferred from the casting to the mold can then be used to find the new casting temperature from Equation 5.23.

$$\rho_c SH(\partial f_s/\partial t) - \rho_c SC_c(\partial T_\infty/\partial t) = -k(\partial T/\partial Z) \quad (7.23)$$

where ρ_c is the casting density, S is the casting thickness, H is the latent heat of solidification, and f_s is the solid fraction.

$$f_s = (T_\infty-T_L)/(T_S-T_L) \quad (7.24)$$

where T_L is the liquidus temperature and T_S is the solidus temperature.

7.4.2. Flux and Concentration Profile Equations

At the metal interface the reaction is assumed to proceed so rapidly that the concentration of water, C_{H2O}, is zero. The flux of water is given by

$$N_{H2O} = -CD(\partial X_{H2O}/\partial Z) + NC_{H2O}/C \quad (7.25)$$

where N_{H2O} is the flux of water, D is the diffusivity, X_{H2O} is the mole fraction of water, N is the total flux and C is the total concentration. Substitution of 0 for C_{H2O} in Equation 5.25 causes the second term on the right hand side to go to zero. Thus N is not required to find N_{H2O} at the interface. X_{H2O} is given by

$$X_{H2O} = C_{H2O}/C \quad (7.26)$$

and the total concentration can be found with the ideal gas law

$$C = P/RT \tag{7.27}$$

where P is the pressure (atm), T is the temperature (K), and R is the ideal gas constant (L-atm/mol-sec). At the interface water reacts to produce H_2, CO, and CO_2. The relative proportions of these products is, however, dependent on the flux of carbon to the interface. The total flux is dependent on the products produced at the interface but to a much lower extent than its dependence on the temperature change. Experiments have shown that the predominant gases produced are H_2 and CO. Therefore we will approximate the flux at the interface as

$$N_{H2O} = -N_{CO} = -N_{H2} \tag{7.28}$$

where N_{CO} is the flux of CO and N_{H2} is the flux of H_2. Therefore

$$N = N_{H2O} + N_{CO} + N_{H2} = -N_{H2O} \tag{7.29}$$

at the metal interface. The flux at the interior nodes can be found by a total mole balance yielding

$$\partial N/\partial Z = \partial C/\partial t \tag{7.30}$$

similarly a balance on water yields

$$\partial N_{H2O}/\partial Z = \partial C_{H2O}/\partial \tag{7.31}$$

7.5. Coupling of Carbon Diffusion Model and Oxygen Flux Model

Using the flux of carbon and the flux of water vapor we can calculate the flux of CO_2 at the interface.

$$N_{CO2} = -N_{H2O} - N_C \tag{7.32}$$

Where N_C is the flux of carbon (the negative sign before N_{H2O} is required because flux from the mold to the interface has a negative value). Of course this is only true if the flux of carbon is within the boundary of 0.5 to one times the flux of water. If the flux of carbon is below this limit an excess of oxygen (from water) is provided to the interface which will likely result directly in the oxidation of iron. If the flux of carbon is greater than this limit a buildup of carbon will occur at the interface and protect the iron from oxidation. Within these limits the ratio of CO_2/CO can be calculated and used to predict the likelihood of iron oxidation and subsequent penetration.

7.6. Results

The computer program successfully produced temperature profiles with minor artifacts resulting from the finite difference technique, as shown in Figure 7-3. The temperature profile of

five nodes spaced four mm apart can be seen with the nodes closer to the interface having higher temperatures at any given time. The discretization artifact arises as the dry sand zone front passes over a nodal position. When this happens the node suddenly begins to change temperature. This causes the profile for the neighboring node to appear bent from what should be a smooth curve.

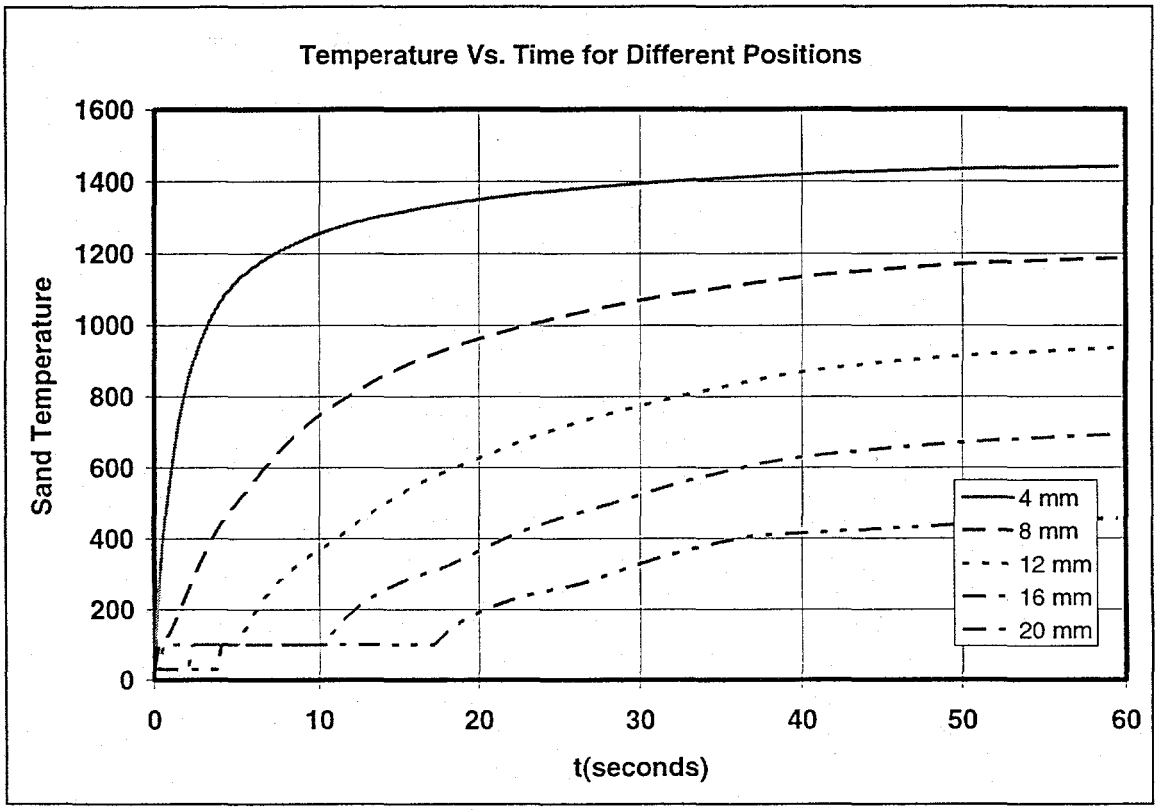

Figure 7-3. Temperature profile of a sand mold calculated with the model.

The CO_2/CO ratios calculated resemble those obtained from foundry experiments with green sand (no carbon) and sodium silicate molds. The program can be used to determine the effect of several variables on the probability of penetration occurring. These variables include pouring temperature, carbon concentration of the steel, moisture content of the mold and diffusivity of gases through the mold (estimated using the sand grain size). The program could also be used to determine the effect (through changing diffusivity) of mold coatings on penetration. However this requires a very small node spacing and resulting time step which lead to long execution times. The CO_2/CO profile produced with the model is very close to that obtained experimentally for times less than five minutes. The conditions used in the green sand with no added carbon experiment were used with the model to produce Figure 7-4.. The model data is that for the first node, 4 mm from the metal surface. The experimental data shown on this plot has been shifted to earlier times coinciding with the model data because of the lag time in collection of this data. This time shift is primarily due to the time required to transport gases from the probe tip to the instrument (45 s) but also due to the time required for gases to diffuse from the metal surface to the probe tip.

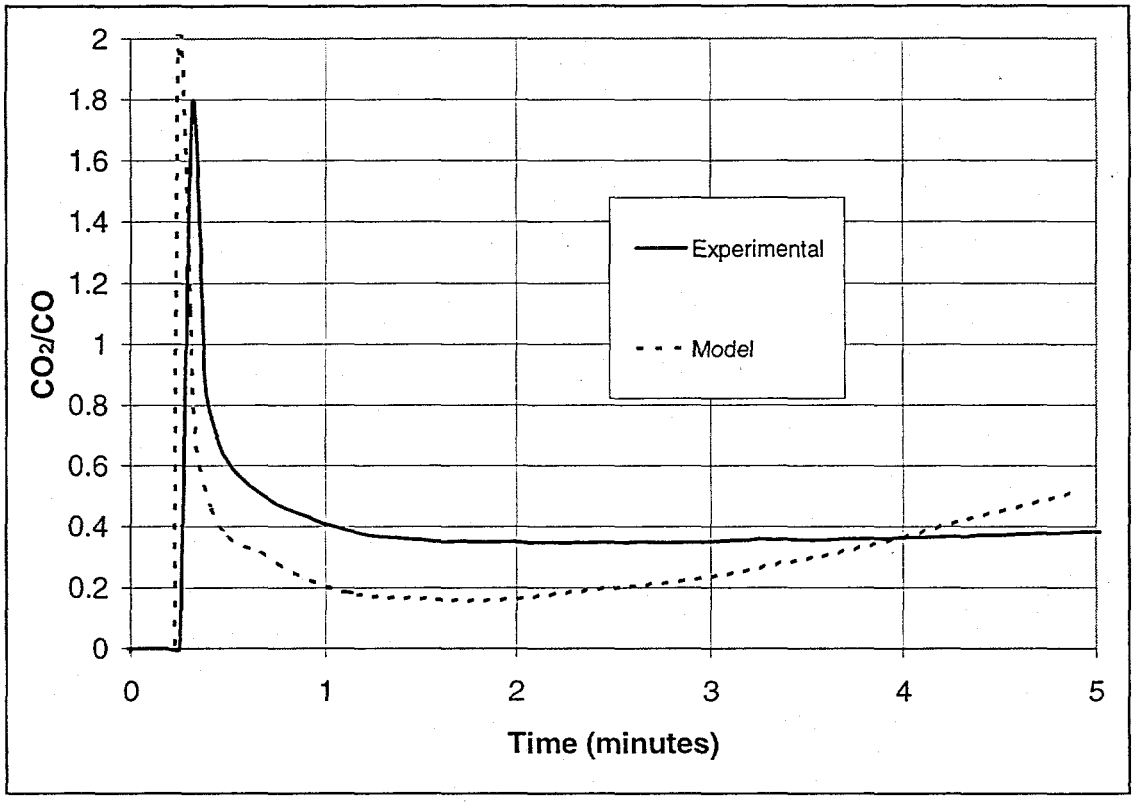

Figure 7-4. CO_2/CO ratio predicted from chemical penetration model and from experiment.

At later times the modeled ratio becomes much higher than that obtained experimentally. This can be explained as follows. Although the gases produced at the interface are highly oxidizing at later times they are produced in very small quantities. Because the experimental probe was placed 1/4" from the interface, the measured gases were actually mixed with the less oxidizing gases present in the bulk of the mold. Since gas production decreases with time the difference between modeled and experimental numbers increases with time. For this reason the model may actually be a better representation of conditions at the interface than the experimental data. The difference in results at later times is not of great concern since penetration occurring after solidification is easily removed.

A plot of the percent carbon contained in the steel at the interface as a function of time is shown in Figure 7-5. Also shown on this plot is the critical carbon content. Whenever the critical percent carbon exceeds the actual carbon content, oxidation of the steel should occur. This figure shows the results obtained using data from the green sand without carbon additions experiment. The model predicts that oxidation of steel will occur at early times resulting in penetration. This is also what was found experimentally. The critical percent carbon also exceeds the actual percent carbon at longer times. This would predict that penetration should also occur after the

casting has solidified but, according to the kinetic study results, should be easily removable. Again this is what was found as discussed in the chapter on measurement of gas compositions.

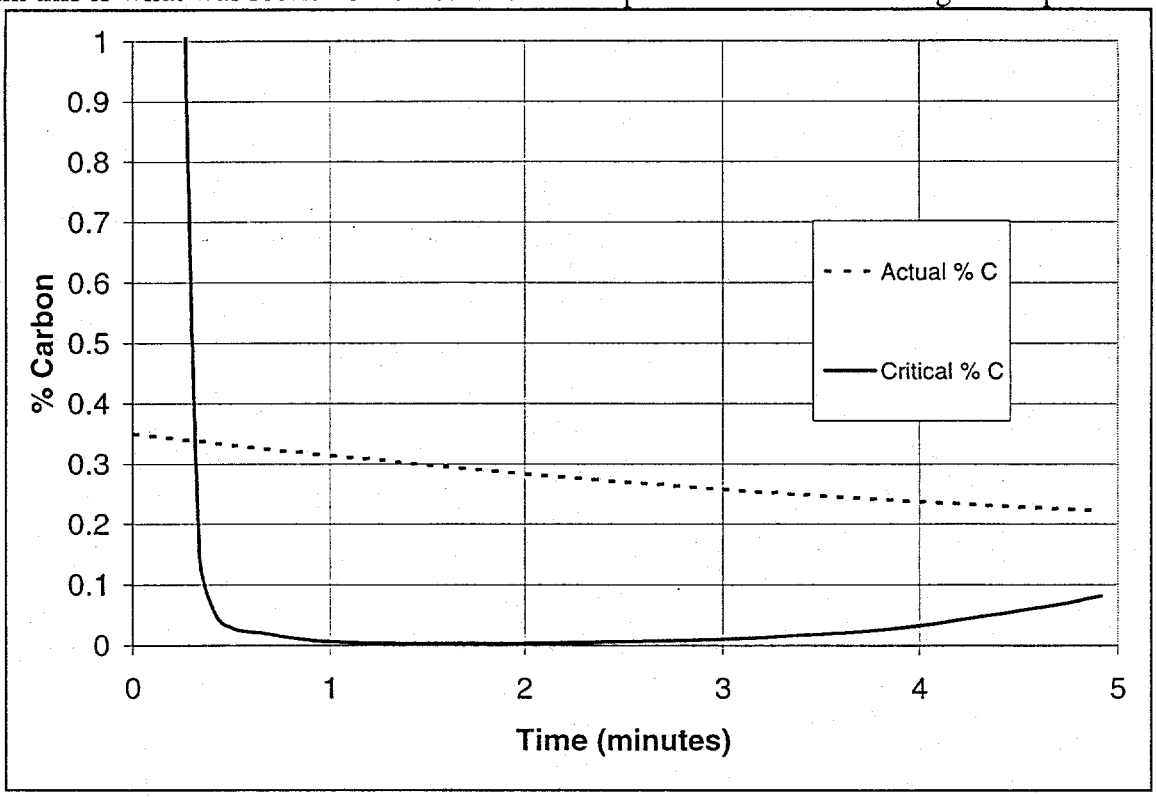

Figure 7-5. Chemical penetration model output for 0.35%C steel

Not surprisingly, it was found that the percent carbon contained in the mold had the greatest effect on penetration. Figure 7-6 shows the results obtained when the original percent carbon in the steel is doubled to 0.7 percent. The critical percent carbon still exceeds the actual percent carbon at the beginning of the experiment but for a much shorter period of time. Thus one could expect penetration to be less severe with higher carbon concentrations.

Lowering the original percent carbon in the steel to 0.2 percent produces an even more dramatic effect as shown in Figure 7-7. This experiment predicts that oxidation and subsequently penetration will occur from the beginning of the experiment through solidification.

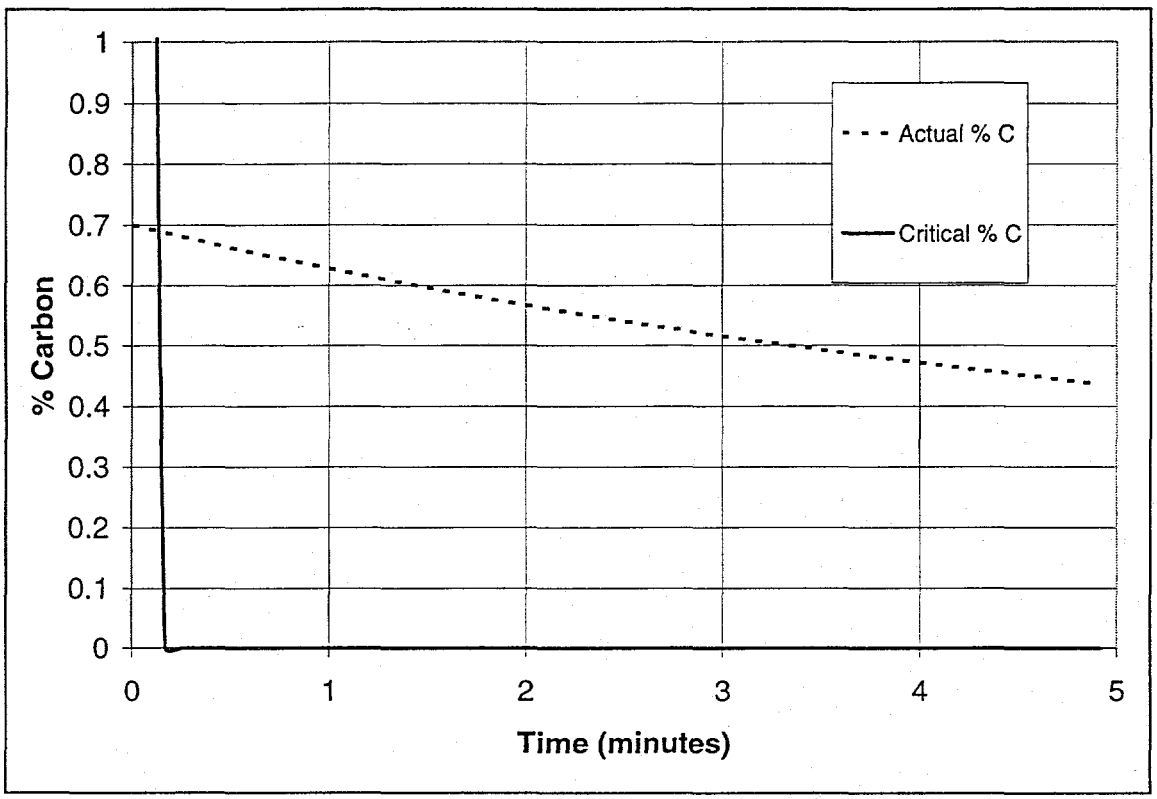

Figure 7-6. Chemical penetration model output for 0.70%C steel

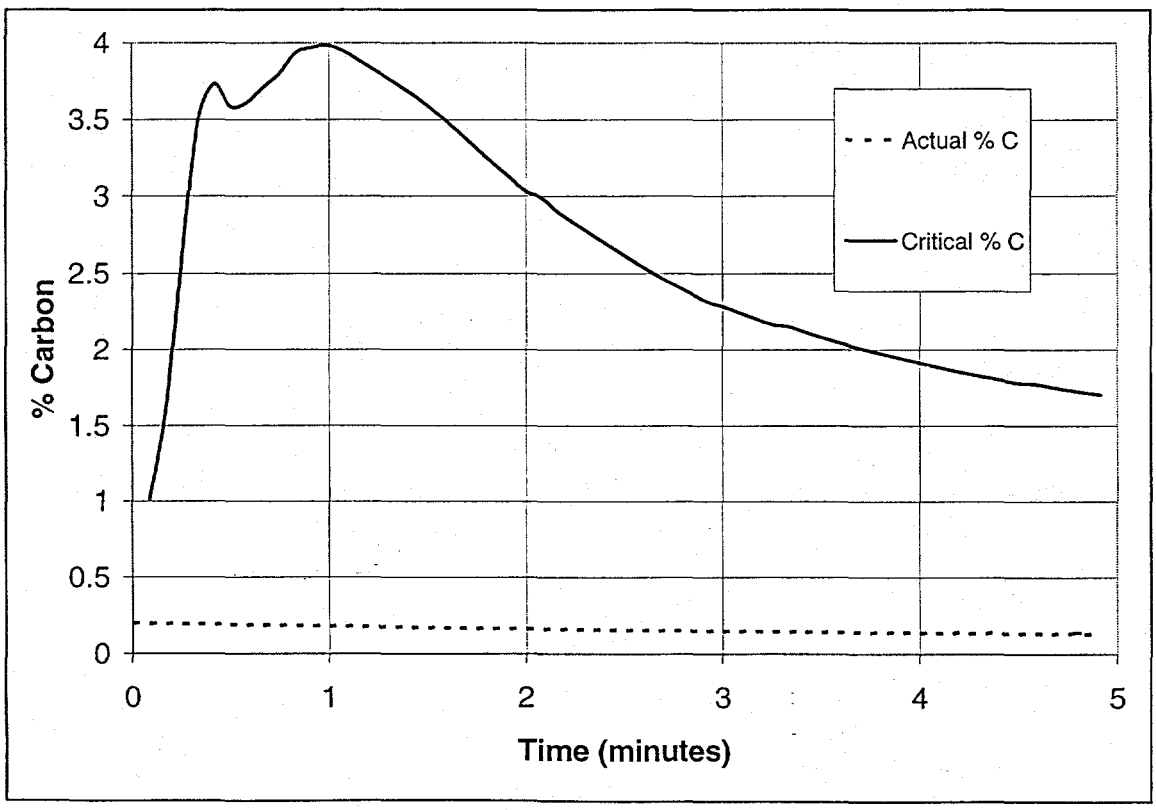

Figure 7-7. Chemical penetration model output for 0.20%C steel

Reasonably small changes in the temperature of the molten metal do not produce significant changes in the profile. Changes in the original moisture content also have a very small effect. Changes in the diffusivity do have a noticeable effect on the profile. Figure 7-8 demonstrates the effect of increasing the diffusivity of water in the mold by 10 percent. All other parameters for this experiment are identical to those used in obtaining Figure 7-5. The model predicts that increasing the diffusivity will increase the period of time in which steel is oxidized at the beginning of the experiment and will also cause the second period of oxidation to begin earlier. In other words, the finer the grain size, the lower the diffusivity, the less chance of chemical penetration.

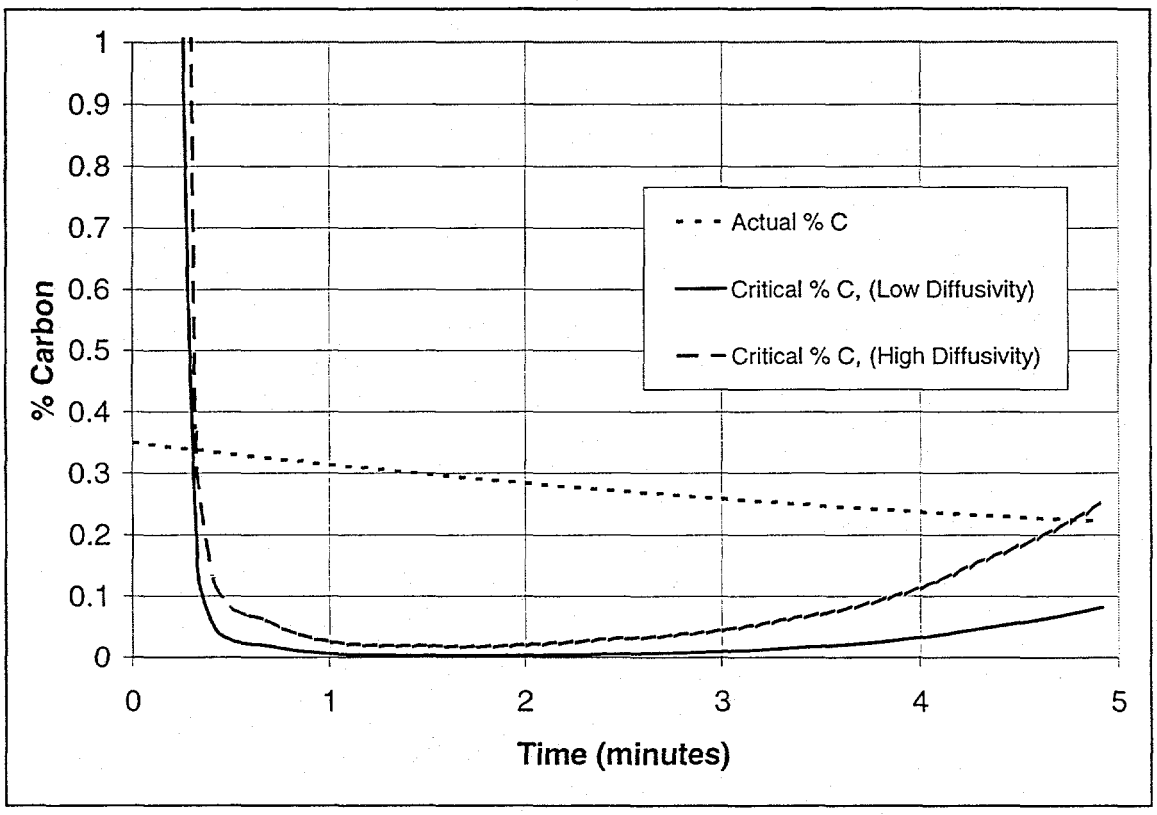

Figure 7-8. Percent carbon in steel at surface, diffusivity of water increased by 10%.

From the previous figures, it can be seen that regardless of the carbon content of steel, penetration will always occur when no seacoal is present in the mold. Figure 7-9, is a graph showing the actual and critical carbon contents for a casting in a resin bonded mold. In this case, the actual carbon content is always larger than the critical carbon content for resin bonded molds. Therefore, chemical penetration will not occur as discovered in the analysis. The data for critical carbon in this figure is from actual data recorded in the mold atmosphere tests because the model is not developed for resin bonded molds.

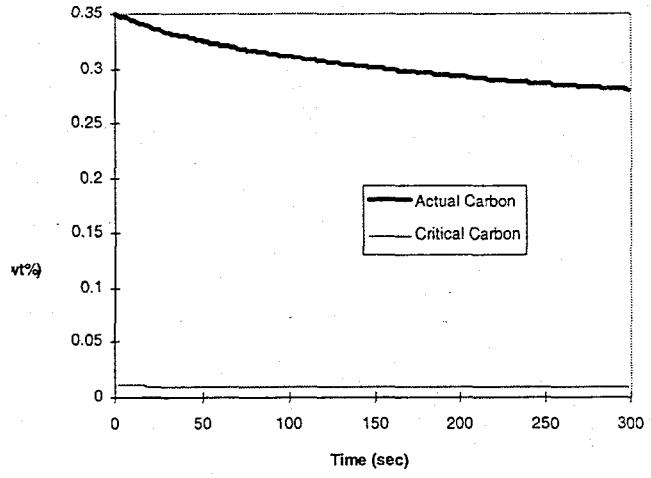

Figure 7-1 Critical carbon and actual carbon contents for casting poured in resin-bonded mold.

7.7. Conclusions

The simplified model produces results that are reassuringly similar to experimental results despite the large number of factors excluded from the model for simplifications. The model for the temperature profile can be used without further modifications. The only shortcomings are the somewhat unrealistic temperature discontinuities produced at the condensation front and the kinks produced in the temperature profile resulting from the discretization. The mass transport model predicts the oxidizing ability of gases at the interface quite well if there is no carbon in the mold. This is precisely where the model has its greatest problem. Since almost all green sand molds are produced with seacoal additions the model is only suitable for those experiments we performed without the additions. The results demonstrate that a model can be produced to predict what will happen in the laboratory. Even the simplified model takes into account the effect of a large number of variables. Those of greatest importance were found to be the concentration of carbon in the steel and the diffusivity of gases through the mold. These results agree well with experience. Higher carbon concentrations in steel decrease the likelihood of penetration as do lower mold permeabilities achieved by using smaller grain sizes and harder ramming.

It is important to realize that this program does not consider all of the factors influencing penetration under actual casting conditions. There is no consideration of seacoal additions to the mold as are normally used. Neither is the influence of other elements contained in the metal considered. A complete model would need to include reactions taking place in the mold that produce a more reducing atmosphere when carbon additions are made. Perhaps even more complicated would be the change in diffusivity which occurs as mold additives swell and/or fuse with increasing temperatures. Finally, the chemistry of minor elements contained in the steel and the effect of their oxidation products on contact angles should be included.

8. Model for Mechanical Penetration

The Mechanical Penetration Prognosticator is designed to predict the occurrence of mechanical penetration in steel castings. It is written in the Visual Basic software language for use with Microsoft Excel version 7.0. Microsoft Excel is the only program needed to run the program. The program utilizes user-inputted variables to determine the likelihood for penetration to occur.

8.1. Introduction

The mechanism of mechanical penetration can be shown by a pressure balance at the mold/metal interface. This pressure balance is shown in Figure 8-1.

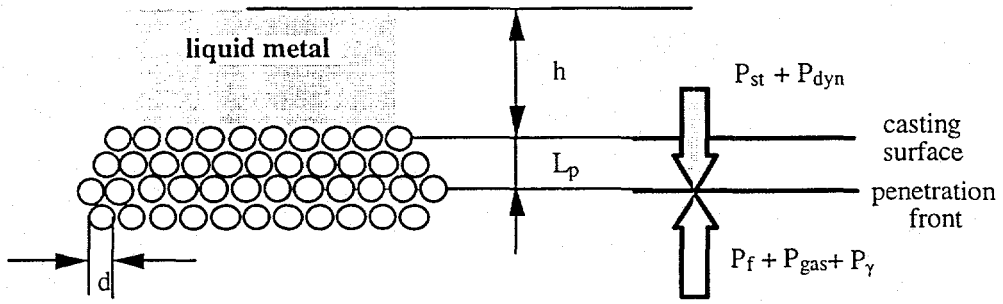

Figure 8-1. Representation of Mechanical Penetration Mechanism

This figure can be expressed in equation form according to:

$$P_{st} + P_{dyn} = P_\gamma + P_{gas} + P_f \tag{8.1}$$

The static pressure (P_{st}) and the dynamic pressure (P_{dyn}) encourage penetration, whereas capillary pressure (P_γ), gas pressure (P_{gas}), and frictional pressure (P_f) oppose it. These pressures are quantified in reference 37. From these equations, a critical contact angle, θ_{cr}, can be calculated according to the following equation:

$$\theta_{cr} = \cos^{-1}\left[\frac{d_e}{4\gamma_{LV}}(\rho g h + \rho V^2)\right] \tag{8.2}$$

where, ρ= density of liquid steel
g= acceleration due to gravity
h= metallostatic head height
V= velocity of metal against the mold wall
d_e= equivalent capillary diameter
γ_{LV}= liquid vapor surface energy

If the contact angle between the steel and molding aggregate is higher than θ_{cr}, penetration is not likely. If it is lower, then penetration is likely.

8.2. Program Inputs

8.2.1. Types of steel

The Mechanical Penetration Prognosticator is designed to be used for the carbon, stainless, and manganese steels tested in the sessile drop experiments. Several assumptions are made for this program: first, the superheating temperature is assumed to be 150 degrees Celsius above the melting temperature; second, the contact angles are a linear function of carbon content for carbon steels; third, the contact angles for stainless and manganese steels do not vary with composition. The final two assumptions are not valid, but are necessary due to the limited amount of data generated in the sessile drop portion of the study.

8.2.2. Types of substrates

The mechanical penetration prognosticator is designed to operate with nine different molding aggregate chemistries. These are silica, zircon, alumina, mullite (60% alumina), mullite (70 % alumina), bauxite, olivine, chromite, and magnesite. These substrates can be either sand grains or refractory coatings.

8.2.3. Mold Variables

The user must input several mold variables or accept the default values. These values are metallostatic head height, metal velocity against the mold wall, and the equivalent capillary diameter measurement. Grain fineness number (GFN), mold quality indicator (MQI), mold hardness, or coating particle size are the choices for this value. The values for metallostatic head and the metal velocity against the mold wall are in British units to comply with sponsor suggestions.

8.2.3.1.Equivalent capillary diameter for sand molds with coatings

To determine the equivalent capillary diameter for sand molds with refractory coatings, several assumptions were made. First, the coating is applied evenly with no vacancies. Second, the coating particles are spherical in shape. Finally, the coating particles are assumed to be all of the same size. The derivation is similar to that of Stefanescu[3] et al., for sand molds. The final equation for the capillary diameter is:

$$d_e = 0.702d \tag{8.3}$$

where d is the average coating particle diameter.

8.3. Program Output

8.3.1. Penetration Index

The mechanical penetration prognosticator uses the variables described above to calculate a penetration index (PI). This index is the ratio of the actual contact angle between the molten steel and the mold aggregate and the critical contact angle according to equation 8.2. The actual contact angle is obtained from the data bank of monolithic steady state contact angles generated in the sessile drop experiments. The equation is as follows:

$$PI = \frac{\theta_{act}}{\theta_{cr}} \tag{8.4}$$

8.3.2. Prediction of Penetration

The penetration index is the variable used to determine whether or not penetration will occur. This determination is as follows:

If PI>1, penetration is not likely to occur.
If PI<1, penetration is likely.
If PI=0, then it is not advised to use the metal/mold combination selected.

8.4. Operation of Program

The mechanical penetration prognosticator is designed to be user friendly. The main screen is shown below:

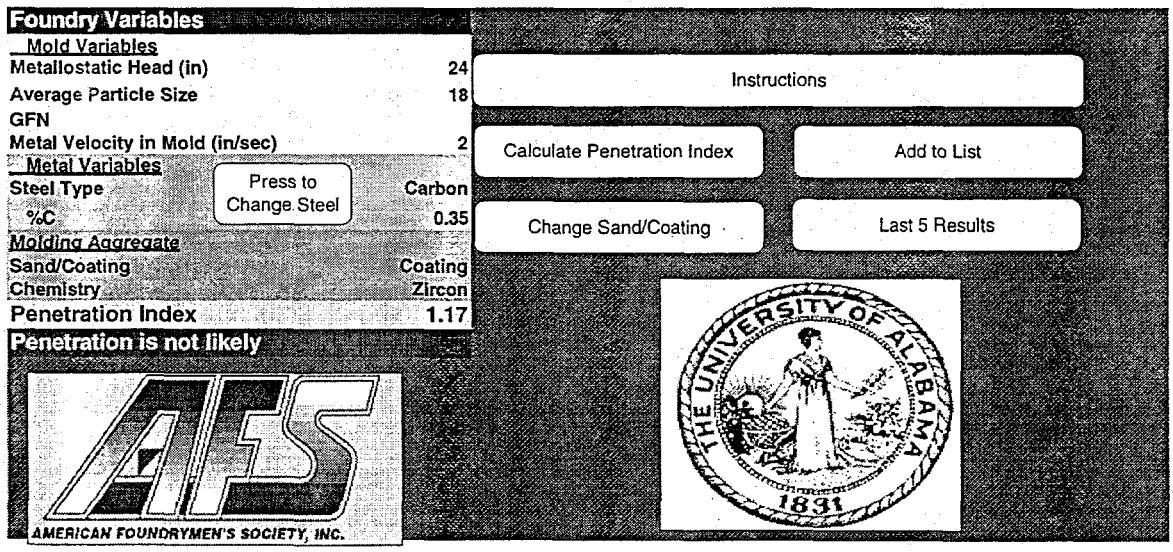

Figure 8-2. Main screen of mechanical penetration prognosticator

The program is activated by selecting one of the six buttons shown on this screen. Each button is detailed in its appropriate section.

8.4.1. Instructions

Selection of the *Instructions* button results in another screen being shown. This screen is simply a detailed list of instructions as how to operate the program. This screen is shown below:

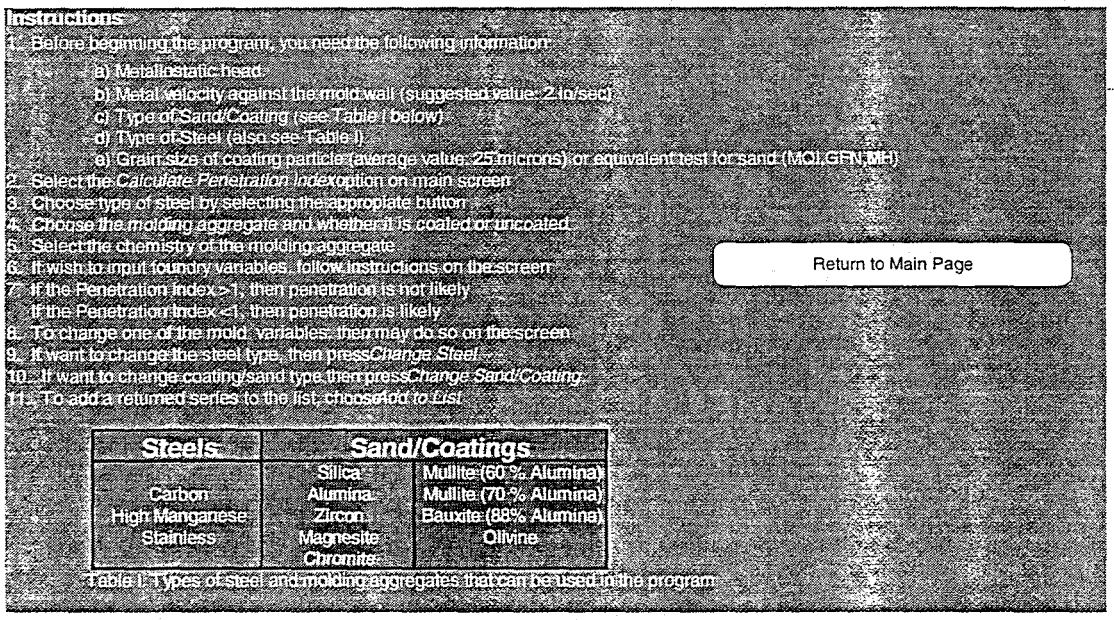

Figure 8-3. Instructions screen of mechanical penetration prognosticator

8.4.2. Calculate Penetration Index

This button allows for the user to be prompted to enter every variable used in the program. First, the user is asked to select the type of steel. If the steel type is carbon steel, then the user is asked to enter the carbon content of the steel. Second, the type of molding aggregate and its chemistry is selected. Then the user is asked whether or not he wishes to enter the foundry variables. If yes, then each value is entered. If no, then default values are assigned. The calculated penetration index is shown on the main screen as is the prediction of penetration.

8.4.3. Change Sand/Coating

This button allows for the user to change the type of molding aggregate. All foundry variable are maintained. However, it should be checked that the correct value for calculation of the capillary diameter is listed. If not, then the correct value should be entered. This button allows for comparison between different molding aggregates.

8.4.4. Change Steel

This button allows for the steel to be changed. This can be either changing the carbon content, or changing the type of steel. Because of the way the program is written, it is necessary to reselect the molding aggregate. All other values are retained. It should also be noted that erroneous results may be obtained if the carbon content is changed directly on the main screen.

8.4.5. Add to List

This button allows for the data on the main screen to be added to a list of the last five results. This allows for data to be gathered to compare the different molding aggregates on screen. Also, it allows for the influence of different variables such as metallostatic head and metal velocity to be seen. This list can also be seen by selecting the button marked *Last 5 Results.* This screen is as follows.

Foundry Variables					
Mold Variables					
Metallostatic Head (in)	100	48	36	24	12
Average Particle Size(microns)	18	18	18	18	18
GFN					
Metal Velocity in Mold (in/sec)	2	2	2	2	2
Metal Variables					
Steel Type	Carbon	Carbon	Carbon	Carbon	Carbon
%C	0.35	0.35	0.35	0.35	0.35
Molding Aggregate					
Sand/Coating	Coating	Coating	Coating	Coating	Coating
Chemistry	Zircon	Zircon	Zircon	Zircon	Zircon
Penetration Index	1.03	1.13	1.15	1.17	1.20

Penetration Index<1; Penetration is Likely
Penetration Index>1; Penetration is not Likely

For Coatings:Values in Row 4 are Average Particle Size
For Sand: Values in Row 4 are either MQI or Mold Hardness

Figure 8-4.Screen showing the last five results obtained from the penetration prognosticator

This example shows how the relationship between metallostatic head and the penetration index for carbon steel (0.35%C) and zircon coating can be seen.

8.5. Results

The mechanical penetration prognosticator can be used to establish relationships between certain variables and the penetration index. One example of this is shown in Figure 8-5.

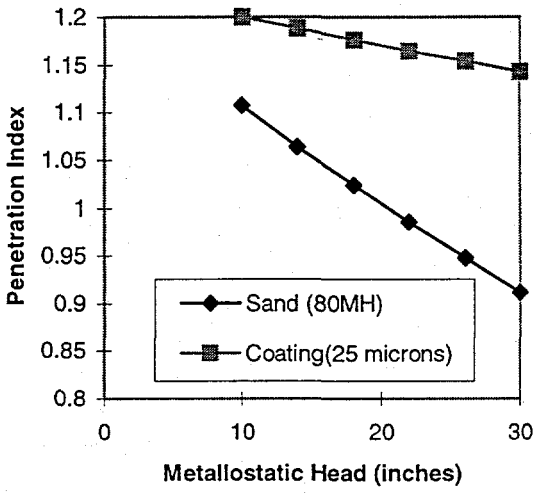

Figure 8-5. Influence of metallostatic head height on the penetration index for both zircon sand and zircon coating. Metal velocity=2 in/sec

In this example it is shown that as the metallostatic head increases, the penetration index decreases. Also shown is the advantage obtained by using a coating to prevent penetration. The penetration index is at approximately 1.15 for the zircon coating and 0.90 for the zircon sand with a metallostatic head of 30 inches. This reveals that a coating allows a substantially metallostatic head height without the risk of penetration.

Another relationship that can be established is the influence of carbon content on the penetration index. This is a direct result of the change in the contact angle values for the different carbon contents. Because of this, this relationship can be different for each metal/molding aggregate combination. Figure 8-6 is an example of the influence of carbon content on the penetration index for carbon steel in a zircon sand mold. The change in the capillary diameter can also have an effect on the penetration index. This is represented in Figure 8-7. The higher the MQI value, the smaller the capillary diameter. Therefore, as the capillary diameter decreases, the penetration index increases.

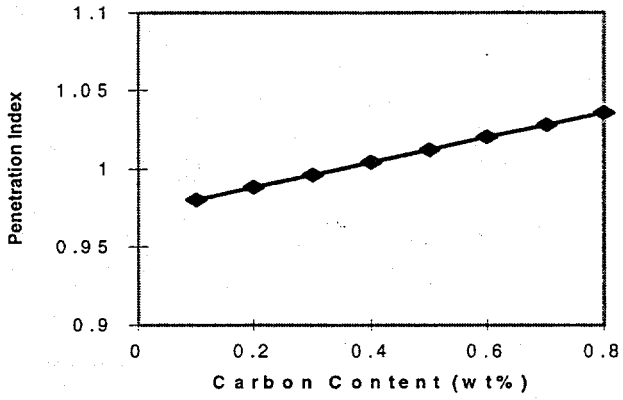

Figure 8-6. Influence of carbon content on penetration index in zircon sand mold (metallostatic head=20 in, metal velocity=2 in/sec, mold hardness=80)

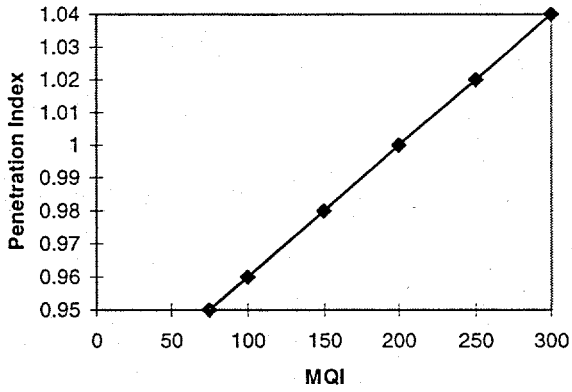

Figure 8-7. Effect of MQI on the penetration index for 0.4%C steel on Bauxite sand (metallostatic head=20 in, GFN=85)

8.6. Validation

The mechanical penetration prognosticator was used to predict the occurrence of penetration in twenty test castings performed at the University of Alabama metal casting laboratory and a participating foundry. The results of these experiments are summarized in Table 8-1.

Table 8-1. Results of Penetration Prognosticator Predictions for UA castings

Number	Coating	wt % C	Penetration	PI	Predicted	Correct
UA1	None	0.28	No	0.97	Yes	No
UA2	Zircon	0.74	No	1.14	No	Yes
UA3	Zircon	0.69	No	1.14	No	Yes
UA4	Mullite	0.71	No	1.07	No	Yes
UA5	None	0.70	Yes	0.99	Yes	Yes
UA6	Mullite	0.72	No	1.06	No	Yes
UA7	Magnesite	0.71	Yes	1.33	No	No
UA8	Magnesite	0.76	No	1.35	No	Yes
UA9	None	0.71	Yes	0.99	Yes	Yes
UA10	Magnesite	0.70	Yes	1.32	No	No
UA11	None	0.72	Yes	0.99	Yes	Yes
UA12	Zircon	0.73	No	1.23	No	Yes
UA13	Mullite	0.70	No	1.06	No	Yes
UA14	None	0.26	Yes	0.96	Yes	Yes
UA15	None	0.25	Yes	0.96	Yes	Yes
UA16	None	0.25	No	0.96	Yes	No
UA17	None	0.38	Yes	0.99	Yes	Yes
UA18	None	0.30	Yes	0.97	Yes	Yes
UA19	None	0.29	Yes	0.97	Yes	Yes
UA20	None	0.24	Yes	0.96	Yes	Yes

As can be seen in Table 8-1, the mechanical penetration prognosticator correctly predicted penetration in sixteen of twenty steel castings. One case in which it incorrectly predicted penetration is UA1. In this case the pouring temperature was low, therefore the penetration index would be higher if the program accounted for different superheating temperatures. Two cases in which penetration was not predicted and it occurred are for castings UA7 and UA10. Both of these castings were coated with magnesite. It is believed that the coating was incorrectly applied resulting in the occurrence of penetration. The only other case of inaccurate prediction is UA16.

9. Conclusions

The research program was successful in identifying the major factors that influence penetration. This was done first through a case study of penetration samples. The study revealed that both chemical and mechanical penetration were present in carbon and high manganese steels. It also found that only mechanical penetration is found in stainless steel samples. It should be noted that when mechanical penetration does occur, there is a greater risk of chemical reactions with the mold. Therefore, it is common to confuse mechanical penetration with chemical.

Sessile drop experiments were run to discover the effect of steel chemistry on the contact angle for different substrates. These experiments revealed the best substrates for each type of metal. Bauxite, magnesite, and mullite were discovered to be the best materials for resisting mechanical penetration. It was also shown that high manganese steels cannot be poured into silica molds and that stainless steel should not be poured in chromite molds. The sessile drop data was used to develop a mechanical penetration model which correctly predicted penetration in sixteen of twenty castings poured at the University of Alabama

Mold/metal atmosphere tests were run to understand the effects of the atmosphere on chemical penetration. It was found that the chemistry affecting penetration has its greatest effect as the casting is just poured. This is because the interfacial gases are most oxidizing at this time, as determined with the model, the gas measurement experiments and simply by reasoning. The high concentration of oxygen atoms initially present in the mold decreases rapidly as steam reacts with carbon to produce hydrogen and carbon monoxide. The rapid expansion of gases caused by reactions and the temperature increase flushes the oxidizing gases away from the interface leaving a more reducing atmosphere. It is during this early time that hard-to-remove penetration is produced.

Chemical penetration for low carbon steels cannot be completely eliminated by adding carbon (seacoal) to green sand molds although a marked decrease is obtained in its severity. Extremely high carbon concentrations might be able to totally eliminate the penetration but are not used because of their possible diffusion into the steel causing carburization. Results with sodium silicate molds were very similar to those obtained with green sand molds without the carbon additions. The cause of penetration is the same, a highly oxidizing atmosphere produced at the beginning of the experiment. Resin bonded molds produced no penetration. This is because the oxidizing gases originally present in the mold are flushed out by the vaporization of organic material. Therefore large concentrations of carbon dioxide are never produced.

A chemical penetration model was produced and its results agree well with the experimental results. The likelihood of penetration is indicated by comparing the concentration of carbon in the steel to a critical carbon concentration required to prevent oxidation of the metal given the oxidizing ability of gases present in the mold. The results show that lower concentrations of carbon in steel and higher diffusivity of water vapor through the mold are more likely to lead to penetration. These are not surprising revelations, but they do indicate the ability of the model to predict the effect of changing variables. Even the simplified model takes into

account the effect of a large number of variables, including moisture content in the mold, pouring temperature, heat transfer coefficient, thermal conductivity, heat capacity and carbon content of the steel. The model can be used to predict the effects of changes in any number of these variables.

Solid state penetration can occur after the steel has solidified. This is caused by the extremely low diffusivity of carbon through solidified steel. Although the flux of water to the interface decreases with time it is still greater than that of carbon through the steel. Thus large castings may be able to continue producing fayalite and iron oxide for long periods of time after solidification. As determined in the kinetic studies, the penetration produced after solidification is easily removed.

10. Future Work

The mechanical penetration model should be expanded to develop more accurate equations for the actual contact angle. This can be done by performing a statistical array of sessile drop experiments. This array should include factors such as chemical composition (C,Si,Mn,P,S), superheating, and section size. The section size can be used to detrmine the solidification time of the casting and this time can be inserted in the second order polynomial equation for the contact angles. The major drawback is that the statistical array will have to be completed on all the substrates. Also, the stainless steel and high manganese steel should have a similar statistical array performed.

The next logical project to make full use of the results to date would be the development of a full chemical penetration model. This would obviously be a major undertaking due to the large number of variables that are needed to accurately model the complex processes that occur in the mold. Because many actual castings include cores, the full model should include at least two dimensions. Even a two dimensional model would only be sufficient for castings of low complexity. Chemical reactions are, in reality, taking place throughout the mold, not just at the interface. This complicates the situation more than what may initially be apparent. Because the temperature decreases rapidly with distance from the metal interface, we cannot assume that reaction kinetics are infinitely fast at all points. The reaction rates will actually vary with both time and position as the mold heats up.

The rate of diffusion is not constant. Coatings are often applied that greatly decrease the diffusivity at the mold surface. These materials may also swell with a temperature increase, causing diffusivity changes with time. The moisture content of the mold also affects diffusivity. Thus it will vary with both time and position as the vapor transport zone moves through the mold. The presence of iron oxide and fayalite may also complicate the model. These reaction products may effectively form a seal at the interface. Thus carbon contained at the steel surface and water contained in the first node of the mold may not react instantaneously because they are not actually in contact with each other.

Other factors concerning the steel seem less important but may also need to be included to obtain a realistic model. Elements contained in the steel besides carbon can also act as sacrificial elements. If any of these elements are present in significant concentrations then their rates of diffusion would have to be considered. The oxides produced could then either help or hinder the penetration problem depending on their contact angle with the mold material.

The addition of these equations for an improved model would also lead to a slower program. It would be advisable to find a more efficient method to perform the required calculations. Other examples for modeling heat and moisture transfer use more refined methods including implicit finite differences and the finite element method.[44,45,46]

11. References

References

[1] Draper, A. L., and J. L. Gaindhar. 1975. The Role of Mold Atmospheres in the Penetration of Steel in Sand Molds. *AFS Transactions*, 83:593-616

[2] Frawley, J. J., W. F. Moore, and A. J. Kiesler. 1974. Simulating Mold-Metal Reactions in a Small Laboratory Test. *AFS Transactions*, 82:561-570

[3] Stefanescu, D. M., T. S. Piwonka, S. Giese, A. Lane. 1993. Metal Penetration in Sand Molds: A Fundamental Approach to Solving the Problem. *AFS Transactions*, 101:789-796

[4] Delannoy, P., D. M. Stefanescu, and T. S. Piwonka. 1990. A Critical Literature Review of Theories for the Formation of Casting Metal Penetration Defects. *AFS Research Report No. 2*, (April): 4

[5] Thorpe, P. J. 1971. Avoidance of Metal Penetration and Sand Burn-on in Iron Castings. *The British Foundryman*, (October):380-481

[6] Levelink, H. G., and F.P. M. A. Julien. 1973. Penetration and Shrinkage by Interaction of Solidifying Cast Iron and the Casting Mold (Part 1). *AFS Cast Metals Research Journal*, (June):56-63

[7] Levelink, H. G., and F.P. M. A. Julien. 1973. Penetration and Shrinkage by Interaction of Solidifying Cast Iron and the Casting Mold (Part 2). *AFS Cast Metals Research Journal*, (September):105-109

[8] Taylor, H. F., and Jose Navarro. 1957. Mold-Metal Interface Reactions. *Foundry*, (December):76-80

[9] Svoboda, J. M. 1994. Mechanisms of Metal Penetration in Foundry Molds. *AFS Transactions*, 102:461-471

[10] Svoboda, J. M., and G. H. Geiger. 1969. Mechanisms of Metal Penetration in Foundry Molds. *AFS Transactions*, 77:281-288

[11] Owusu, Y.A., and A. B. Draper. 1978. Metamorphic Zones in Green Sand Molds Poured with Steel. *AFS Transactions,* 86:589-598

[12] Wagner, C. G. 1979. Observations on the Penetration of Steel Into High Density Clay Bonded Molds With Controlled Atmospheres. *AFS Transactions*, 87:573

[13]Scott, W. D., and C.E. Bates. 1975. Decomposition of Resin Binders and the Relationship Between Gases Formed and the Casting Surface Quality. *AFS Transactions*, 83:519.

[14] Scott, W. D., and C.E. Bates. 1976. Decomposition of Resin Binders and the Relationship Between Gases Formed and the Casting Surface Quality Part 2 - Gray Iron. *AFS Transactions*, 84:793-804.

[15] Scott, W. D., and C.E. Bates. 1977. Decomposition of Resin Binders and the Relationship Between Gases Formed and the Casting Surface Quality Part 3. *AFS Transactions*, 85:209-226.

[16] Scott, W.D., P. A. Goodman, and R. W. Monroe. 1978. Gas Generation at the Mold-Metal Interface. AFS Transactions, 86:599-610

[17]Pattabhi, R., A. M. Lane and T. S. Piwonka. 1995. Cast Iron Penetration in Sand Molds Part III. *AFS Transactions*, 103:

[18] Sun, Haiping and Robert D. Pehlke. 1996. Modeling and Experimental Study of Gaseous Oxidation of Liquid Iron Alloys. *Metallurgical and Materials Transactions B,* 27B:854-864.

[19]Bates, C. E., and R. W. Monroe. 1981. Mold Binder Decomposition and its Relation to Gas Defects in Castings. *AFS Transactions*, 83: 671.

[20]Bindernagel, I., A. Kolorz, and K. Orths. 1976. Controlled Additions of Hydrocarbon Components to Molding Sand Mixtures Improve Casting Surface Finish. *AFS International Cast Metals Journal*, (December):43

[21]Emmons, R. C., and J. Bach. 1955. Steel Penetration. *Foundry*, (April):108-116

[22] Savage, Robert E., and H. F. Taylor. 1950. Fayalite Reaction in sand Molds used for Making Steel Castings. *AFS Transactions*, 58:564-577

[23]Goodale, P.L. 1930. Notes on Behavior of sand Molds in Steel Foundries. *AFS Transactions*, 38: 471.

[24]Chakraborty, M., B. K. Dhindaw, and R. Kher. 1986. Mould-metal reactions in casting high manganese steel in sodium silicate bonded sand moulds. *The British Foundryman*, (June):229-234

[25]Lewandowski, Jan Lech, and M. Holtzer. 1995. An Investigation of Wettability and work of Adhesion in Ferrous Alloy Moulding Sand Systems. *Cast Metals*, 8:159-165

[26]Scheffer, K. D. 1975. Behavior of Chromite in Steel Casting Molds and Cores. *AFS Transactions*, 16:585.

[27]Suzuki, K., and S. Nakada. 1976. Resistance to Metal Penetration of Chromite Sand for Steel Castings. *AFS Transactions*, :183-192

[28]Vingas, G. J. 1986. Mold and Core Coatings: Past, Present, and Future. *AFS Transactions*, 81:463

[29]Naro, R. L., and R. D. Tenaglia. 1978. Influence of Nobake Binder Processing Variables on Metal Penetration in Gray Iron Castings. *AFS Transactions*, 28:343

[30]Naro, R. L., and R. D. Tenaglia. 1979 Influence of No Bake Binder Processing Variables on Metal Penetration in Steel Castings. *AFS Transactions*, 24:145

[31]Marek, C. T. 1963. Transformation Zones in Green Sand. *AFS Transactions*, 71:185-192

[32]Marek, C. T. 1965. Effect of Transformation Zones on Casting Problems. *AFS Transactions*, 73:134-141

[33]Draper, A. B. 1969. Condensation Zones in Molding Sands Bonded with Southern Bentonite. *AFS Transactions*, 77:407-414

[34]Campbell, John. 1993. *Castings*. New York: Butterworth Heinemann

[35] American Ceramic Society, *Phase Diagrams for Ceramists*. p.54.

[36] D.M. Stefanescu, P. Delannoy, and T.S. Piwonka, "An Investigation in the Role of Sand-Metal Contact Angle in the Formation of Casting Penetration Defects." *AFS Transactions*, vol. 99, 1991, pp. 761-780.

[37] D.M. Stefanescu, T.S. Piwonka, S.R. Giese, and A. Lane, "Metal Penetration in Sand Molds - A Fundamental Approach to Solving the Problem." *AFS Transactions*, vol. 101, 1993.

[38]Pattabhi, R., "Measurement of Mold/Metal Interface Gas Compositions in Green Sand Molds," M.S. Thesis, The University of Alabama, 1995.

[39]Hernandez, B., and J. F. Wallace. 1978. Mechanism of Pinhole Formation in Gray Iron. *AFS Transactions*, 33:335

[40]Crank, J. 1975. *The Mathematics of Diffusion.* 2nd ed. New York: Oxford University Press.

[41]Reed-Hill, R. E. and Abbaschian. 1994. Physical Metallurgy Principles. 3rd ed. Boston: PWS Publishing Co.

[42]Tsai, H. L., K. C. Chiang, and T. S. Chen. 1988. Movement of Moisture Front and Alloy Solidification in Green Sand Casting. *AFS Transactions*, 96:191-196

---

[43]Incropera, F. P. and D. P. DeWitt. 1990. *Fundamentals of Heat and Mass Transfer.* 3rd Ed. New York: John Wiley and Sons

[44]Kubo, and R. D. Pehlke. 1986. Heat and Moisture Transfer in Sand Molds Containing Water. *Metallurgical Transactions B*, 17B:903-911.

[45]Gu, L., M. V. Swami, and P. Fairey. 1993. Generalized Theoretical Model of Combined Heat, Air and Moisture Transfer in Porous Media. *Multiphase Transport in Porous Media ASME*, 173:47-54

[46]Hou, T. X., R. D. Pehlke, and J. O. Wilkes. 1991. Solidification Modeling: Reduction of Computing Time in the Mold Region. *AFS Transactions*, 99:325-332